Contrib Mineral Petrol (2009) 157:429–451
DOI 10.1007/s00410-008-0344-7

ORIGINAL PAPER

An experimental study of focused magma transport and basalt–peridotite interactions beneath mid-ocean ridges: implications for the generation of primitive MORB compositions

Sarah Lambart · Didier Laporte · Pierre Schiano

Received: 17 March 2008 / Accepted: 4 September 2008 / Published online: 25 September 2008
© Springer-Verlag 2008

Abstract We performed experiments in a piston-cylinder apparatus to determine the effects of focused magma transport into highly permeable channels beneath mid-ocean ridges on: (1) the chemical composition of the ascending basalt; and (2) the proportions and compositions of solid phases in the surrounding mantle. In our experiments, magma focusing was supposed to occur instantaneously at a pressure of 1.25 GPa. We first determined the equilibrium melt composition of a fertile mantle (FM) at 1.25 GPa-1,310°C; this composition was then synthesised as a gel and added in various proportions to peridotite FM to simulate focusing factors Ω equal to 3 and 6 (Ω = 3 means that the total mass of liquid in the system increased by a factor of 3 due to focusing). Peridotite FM and the two basalt-enriched compositions were equilibrated at 1 GPa-1,290°C; 0.75 GPa-1,270°C; 0.5 GPa-1,250°C, to monitor the evolution of phase proportions and compositions during adiabatic decompression melting. Our main results may be summarised as follows: (1) magma focusing induces major changes of the coefficients of the decompression melting reaction, in particular, a major increase of the rate of opx consumption, which lead to complete exhaustion of orthopyroxene (and clinopyroxene) and the formation of a dunitic residue. A focusing factor of ≈4—that is, a magma/rock ratios equal to ≈0.26—is sufficient to produce a dunite at 0.5 GPa. (2) Liquids in equilibrium with olivine (±spinel) at low pressure (0.5 GPa) have lower SiO_2 concentrations, and higher concentrations in MgO, FeO, and incompatible elements (Na_2O, K_2O, TiO_2) than liquids produced by decompression melting of the fertile mantle, and plot in the primitive MORB field in the olivine–silica–diopside–plagioclase tetrahedron. Our study confirms that there is a genetic relationship between focused magma transport, dunite bodies in the upper mantle, and the generation of primitive MORBs.

Keywords Dunite · Peridotite · Partial melting · Focused magma transport · Primitive MORB · Magma/rock interactions

Communicated by T.L. Grove.

S. Lambart (✉) · D. Laporte · P. Schiano
Laboratoire Magmas et Volcans, OPGC, Université Blaise Pascal, CNRS, IRD, 5 rue Kessler, 63038 Clermont-Ferrand Cedex, France
e-mail: S.Lambart@opgc.univ-bpclermont.fr

Introduction

In their source regions, basaltic liquids are in equilibrium with olivine (ol) + orthopyroxene (opx) ± clinopyroxene (cpx) ± spinel (sp) or garnet (grt) depending on pressure (O'Hara 1968; Elthon 1979; Green et al. 1979). However, primitive mid-ocean ridge basalts (MORBs), derived from magmas formed by partial melting of the upper mantle peridotites, are not in equilibrium with this assemblage at any pressure (e.g., O'Hara 1965; Stolper 1980): they are consistently undersaturated in opx and significantly too rich in cpx (diopside) component. Figure 1 shows the major element composition of ~9,000 glasses from the global MORB database, projected from plagioclase in the pseudo-ternary diagram olivine–diopside–silica. Liquids close to equilibrium with mantle olivine (that is, with a molar mg-number Mg# ≥ 67 [Mg# is the molar ratio $Mg^{2+}/(Mg^{2+}+Fe^{2+})$], as shown by the shaded field; e.g., Hess 1992) are consistently opx undersaturated, and plot either within the cpx field in the olivine–diopside–silica

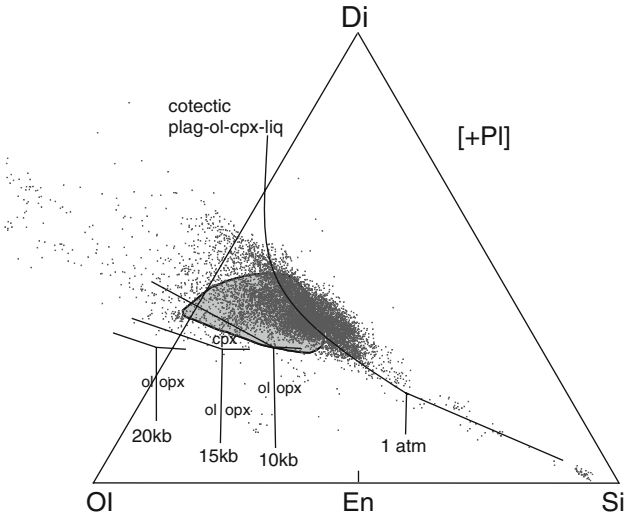

Fig. 1 A comparison of MORB compositions with the phase boundaries in a peridotite at 1 atm, 1, 1.5, and 2 GPa in the olivine–diopside–silica–plagioclase normative tetrahedron (liquid compositions are projected from plagioclase onto olivine–diopside–silica plane). Small dots correspond to 9,035 MORB glass analyses from the Smithsonian Institution catalogue (Melson and O'Hearn 2003: http://www.petdb.org/petdbWeb/index.jsp). The *shaded field* represents the range of primitive MORBs and corresponds to the 61 most primitive MORB glasses from the database with Mg# $\geq$ 67 (total Fe calculated as FeO). From Stolper (1980), with modifications; the algorithm used to calculate the projection is given in Walker et al. (1979)

plane (at high pressures, for instance 1 GPa in Fig. 1) or in the ol field at lower pressures. This observation reflects the fact that MORB compositions are probably not only controlled by partial melting processes deep in the mantle. Indeed, the following processes could modify the chemical composition of primary magmas: (1) magma-rock interactions en route to the surface (Quick 1981; Dick 1989), (2) low pressure crystallization (O'Hara 1965, 1977) and mixing processes that occur within the oceanic crust (O'Hara and Mathews 1981), and (3) high pressure crystallization of primary magmas during their ascent in the upper mantle (Elthon 1987). Although all the processes mentioned above may affect significantly the major element composition of primitive MORBs, in this study we limit our consideration to the effect of magma-rock interactions in the upwelling mantle. As the liquidus volume of olivine in the olivine–silica–diopside–plagioclase tetrahedron increases significantly with decreasing pressure (Stolper 1980; Fig. 1), liquids formed by partial melting at high pressure become increasingly undersaturated in pyroxene during their ascent and tend to dissolve pyroxenes in surrounding peridotites. The effect of magma-rock interactions and pyroxene dissolution will be particularly significant in the case of magma ascent by porous flow: it can result in the formation of high-porosity dunitic channels, which may play a major role in magma transport beneath mid-ocean ridges (Kelemen et al. 1995).

Interaction processes between basalts and their host peridotites and the concomitant formation of dunite channels have been the subject of several geological (e.g., Kelemen et al. 1995; Suhr et al. 2003; Tommasi et al. 2004), theoretical (Asimow and Stolper 1999; Suhr 1999), and experimental (Kelemen et al. 1990; Daines and Kohlstedt 1994; Morgan and Liang 2003, 2005) studies. Some authors have proposed that dunite bodies in mantle peridotites are magmatic, which are formed by the precipitation of olivine into dikes during magma ascent (Quick 1981; Takahashi 1992). Others have suggested that they have a residual origin, and result either from the extraction of very high melt fractions (Jackson and Ohnenstetter 1981) or from melt-rock interactions (Kelemen et al. 1990). According to Kelemen et al. (1997), most dunite bodies were formed at low to moderate pressure (<1.5 GPa) by complete dissolution of pyroxene in peridotites due to focused magma ascent into highly permeable channels. Daines and Kohlstedt (1994) and Spiegelman et al. (2001) showed that the transition from pervasive porous flow to focused magma transport in a network of dunite channels is a consequence of reactive fluid flow and pyroxene dissolution, and is enhanced by solid compaction, which forms impermeable regions between channels. Magma transport beneath mid-ocean ridges would thus mainly occur in highly permeable channels rather than in dikes or by porous flow at low melt fraction in a homogeneous mantle. Such a model can account for both the occurrence of dunites with variable shapes and sizes in large peridotite massifs such as in the Oman ophiolite (e.g., Suhr et al. 2003) and the fact that MORBs are not in equilibrium with a lherzolitic or harzburgitic assemblage at low pressure. Accordingly, the final composition of mantle melts would be controlled by equilibrium with olivine only (or ol + sp) in the dunite channels. Phase compositions in dunites give further support to this hypothesis, as the mg-number of olivine [Ol-Mg#] and the cr-number of spinel [Sp-Cr#, that is the molar ratio $Cr^{3+}/(Cr^{3+}+Al^{3+})$ in sp] in dunites are in equilibrium with MORB compositions (e.g., Kelemen et al. 1995; Tommasi et al. 2004).

A few experimental studies have been carried out to better understand the interactions between basalt and host peridotite and the formation of dunites (Kelemen et al. 1990; Morgan and Liang 2003, 2005). They usually consisted in putting together a peridotite cylinder and a basalt cylinder and to determine the kinetics of interactions between the two components. These studies provided notably a better understanding of the processes operating at the interface between dunite and its host. For instance, Morgan and Liang (2003) showed that the sharp mineralogical front at the dunite-harzburgite interface, observed in a

lot of peridotite massifs and ophiolites (e.g., Kelemen et al. 1995; Takahashi 1992; Kubo 2002; Suhr et al. 2003; Braun and Kelemen 2002), results from a combined effect of orthopyroxene and olivine dissolution at the dunite-harzburgite interface, olivine re-precipitation within the dunite, as well as diffusive exchange between the crystals and the melts. Nevertheless, the application to natural cases is complicated by scaling problems. Morgan and Liang (2003) suggested that diffusive dissolution alone is unable to produce large dunite bodies and that prevalent melt percolation is required in the formation of large dunite channels in the mantle.

To constrain further the magma/rock ratios required to produce dunites during melt/rock interaction processes, we performed piston-cylinder experiments that simulate schematically focused magma transport beneath mid-ocean ridges. Due to the difficulty in reproducing experimentally a process as complex as continuous magma focusing in the ascending mantle (Asimow and Stolper 1999), we considered a simplified model of decompression melting, magma focusing and transport, whose main steps are (Fig. 2):

1. The mantle follows an adiabatic decompression path with a potential temperature of 1,350°C. We chose this value, because it is close to the potential temperature estimated for the source regions of N-MORBs (McKenzie and O'Nions 1991), and to the potential temperature (1,300°C) used by Asimow and Stolper (1999) in most of their calculations on steady-state mantle-melt interactions. From the solidus to 1.25 GPa (a value which corresponds to a degree of melting close to 10%), the mantle evolves as a closed system, and the degree of melting, f, increases steadily with decreasing pressure.
2. A single event of magma focusing is assumed to occur at $P = 1.25$ GPa and $T = 1{,}310$°C, when the degree of melting is close to 10%; at this pressure, lateral migration of partial melt gives rise to channels enriched in liquid separated by domains depleted in liquid. Upon focusing, the total mass of partial melt in a "channel" is multiplied by a factor Ω, hereafter referred to as the 'focusing factor', that is, the mass fraction of liquid increases from f to $\Omega f/(\Omega f + 1 - f)$. The magma/rock ratio—defined as the mass of liquid added to a unit mass of partially molten peridotite at the focusing level—is equal to $(\Omega - 1)f$.
3. From 1.25 GPa to a pressure fixed to 0.5 GPa in the present set of experiments, the system evolves at chemical equilibrium and is closed. The degree of melting increases steadily with decreasing pressure as in step (1), but, at any pressure, f is much larger in the channels than in the original mantle composition due to the effect of focusing. As we show below, focusing eventually leads to the disappearance of pyroxenes, and to the formation of ol + liquid ± sp assemblages, even for magma/rock ratios ≤0.5.
4. At 0.5 GPa, we supposed that the liquid is extracted from the solid matrix to form dikes. Our assumption is that, at some low pressure, the main transport mechanism switches from permeable flow in high-porosity channels to magma transport in dikes, in relation to rheological and thermal changes associated with the transition from a convective regime in depth to a regime of conductive cooling towards the surface (e.g., Niu and Hékinian 1997). The choice of 0.5 GPa is somewhat arbitrary at this stage, and will be discussed later.

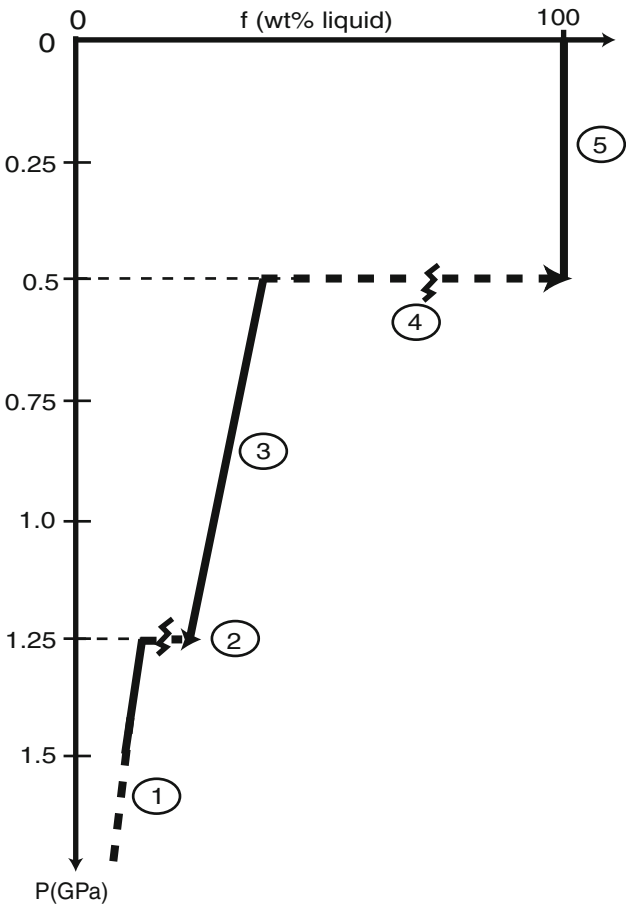

Fig. 2 Evolution of melt fraction, f, as a function of pressure in our simplified model of decompression melting, magma focusing and transport beneath mid-ocean ridges (steps 1–5 are explained in the text). There are two major discontinuities in this model: (1) a discrete event of magma focusing is assumed to occur at $P = 1.25$ GPa; and (2) at 0.5 GPa, the main transport mechanism is supposed to switch from permeable flow in high-porosity channels to magma transport in dikes. In this model, primitive MORB compositions are supposed to correspond to liquids last equilibrated with ol ± sp in the upper part of dunite channels, and then rapidly transported to the surface with minor modifications

5. Finally, the last step of the model is a rapid ascent of magmas in dikes to a shallow chamber beneath the mid-ocean ridge; thus, primitive MORB compositions would correspond to liquids last equilibrated with ol ± sp in the upper part of the dunite channels, and then rapidly transported to the surface with minor modifications.

Due to technical requirements, we had to make the assumption of a closed system behaviour during step (3); this is the main limitation of our study because it implies an absence of relative movement of liquid and solid matrix in the highly permeable channels. Accordingly, the main objective of our work is not to reproduce exactly focused magma transport, but to equilibrate systems corresponding to different focusing factors at various *P* and *T*, in order to characterise the effect of magma/rock ratio on liquid compositions and modal percentages, assemblages, and compositions of solid phases. The ultimate goal is to constrain the magma/rock ratios required to consume all pyroxenes in host peridotites and produce primitive MORB-type liquids in equilibrium with ol ± sp.

Experimental and analytical techniques

Experimental rationale

We first ran an experiment using fertile mantle FM (Table 1) as starting material to determine the equilibrium melt composition at 1.25 GPa-1,310°C (experiment FM1); it enabled us to define the initial state of system, just before melt focusing. This melt composition was then synthesised as a gel and added in various proportions to FM to simulate focusing factors of 3 and 6 (compositions FF3 and FF6, respectively). Compositions FF3 and FF6 were equilibrated at three different *P*–*T* sets along an adiabatic decompression path: 1 GPa-1,290°C; 0.75 GPa-1,270°C and 0.5 GPa-1,250°C (Table 2). Three experiments were performed with composition FM at the same *P* and *T* conditions to characterise the evolution of the system in the absence of focusing ($\Omega = 1$).

Starting materials

Fertile mantle composition FM (Table 1) was prepared by adding 1.4 wt% of synthetic basalt to a powdered spinel peridotite from Mont Briançon, French Massif Central (Laporte et al. 2006). The mixture was first homogenised under ethanol in an agate mortar, and ground to a typical grain size of 2–4 μm using an agate micronizing mill. It was then fired for 6 h at 900°C in a CO_2/H_2 atmosphere with gas flow rates adjusted to yield an oxygen fugacity between the magnetite–wüstite and the iron–wüstite buffers ($f_{O_2} = 10^{-15.91}$bar).

Table 1 Compositions of starting materials (wt%)

	FM[a]	Syn B[b]	FF3[c]	FF6[c]
SiO_2	44.8	48.52	45.42	45.99
TiO_2	0.14	0.87	0.25	0.36
Al_2O_3	4.08	16.57	5.95	7.90
Cr_2O_3	0.48	0.12	0.43	0.37
FeO	8.01	7.16	7.89	7.75
MnO	0.13	0.14	0.13	0.13
MgO	38.62	11.42	34.55	30.30
CaO	3.26	11.69	4.52	5.84
Na_2O	0.35	3.01	0.75	1.16
K_2O	0.04	0.5	0.11	0.18

All compositions are normalised to a sum of 100%

[a] Fertile mantle composition FM analysed by ICP-AES at the Service d'Analyses des Roches et Minéraux (CRPG, Nancy, France)

[b] Composition of the synthetic basalt (analysed by ICP-AES at Laboratoire Magmas et Volcans) added to fertile mantle FM to produce starting compositions FF3 and FF6; Syn B matches the composition of the equilibrium partial melt analysed in run FM1 (1.25 GPa, 1,310°C; "gl_{bottom}" in Table 3)

[c] Compositions produced by mixing mantle FM and synthetic basalt syn B in weight proportions 0.85:0.15 (FF3; $\Omega = 3$) and 0.69:0.31 (FF6; $\Omega = 6$)

A basalt matching the composition of the equilibrium partial melt analysed in run FM1 at 1.25 GPa-1,310°C (Syn B in Table 1) was synthesised as a gel, fired at the same *T* and f_{O_2} as above, and finally added to powder FM to produce starting materials FF3 and FF6 (Table 1). All powders were stored under vacuum to minimise the adsorption of water.

Experimental techniques

The experiments were made in a non-end-loaded, 314-inch piston-cylinder apparatus; *P*-*T* and run durations are summarised in Table 2. We used double containers made of a graphite crucible fitted into a platinum capsule (see Fig. 1 in Laporte et al. 2004). The graphite container was loaded with 20.4–23.8 mg of starting powder, and then put into the platinum capsule and covered with a graphite lid. The platinum capsule was dried in an oven at 300°C for 24 h and then rapidly welded shut while still hot. From the outside to the inside, our piston-cylinder assemblages consist of a NaCl cell wrapped in a lead foil, an outer Pyrex cylinder, a graphite furnace, an inner Pyrex cylinder, a rod of crushable MgO above the platinum capsule, and a sheath of crushable MgO (below the capsule), into which the thermocouple is stuck. The thermocouple tip is separated from the platinum capsule

Table 2 A summary of run information: focusing factor, pressure, temperature, duration *t*, phase assemblages and modes

Run	Ω	*P* (GPa)	*T* (°C)	*t* (h)	Phase assemblage and mode (wt%)[a]				
					Liquid	Ol	Opx	Cpx	Sp
FM-1	1	1.25	1,310	94	8.8 (9)	58.3 (19)	21.0 (41)	11.1 (30)	0.8 (3)
FM-2		1	1,290	72	15.3 (13)	59.8 (21)	19.6 (47)	4.7 (36)	0.6 (3)
FM-3		0.75	1,270	98.5	20.0 (7)	62.1 (12)	17.6 (17)	Absent	0.4 (1)
FM-4		0.5	1,250	119	22.4 (6)	65.3 (9)	12.1 (13)	Absent	0.2 (1)
FF3-0[b]					22.4 (9)	49.6 (19)	17.9 (41)	9.4 (30)	0.7 (3)
FF3-3	3	1	1,290	97.3	26.5 (7)	52.7 (11)	14.0 (25)	6.5 (18)	0.3 (2)
FF3-2		0.75	1,270	99	33.6 (12)	57.9 (18)	8.1 (15)	Absent	0.4 (1)
FF3-1		0.5	1,250	107.5	36.4 (7)	62.1 (11)	1.2 (19)	Absent	0.3 (1)
FF6-0[b]					36.7 (9)	40.5 (19)	14.6 (41)	7.7 (30)	0.5 (3)
FF6-3	6	1	1,290	109	44.1 (15)	46.8 (22)	5.2 (46)	3.7 (28)	0.2 (2)
FF6-2		0.75	1,270	100.5	47.5 (12)	50.7 (17)	0.1 (32)	1.5 (18)	0.4 (2)
FF6-1		0.5	1,250	113.5	51.0 (5)	49.0 (4)	Absent	Absent	Absent

[a] Modes are calculated using a mass balance program modified from Albarède and Provost (1977). The numbers in parentheses are 2σ standard deviations, given in terms of the least unit cited: e.g., 8.8 (9) and 58.3 (19) represent 8.8 ± 0.9 and 58.3 ± 1.9, respectively

[b] The theoretical modes just after the focusing event at 1.25 GPa, 1,310°C are given in the lines FF3-0 and FF6-0. They were calculated from the modes in the partial melting experiment FM1, taking in account the addition of 2 × 0.088 mass of liquid to 1 mass of mantle FM in composition FF3, and 5 × 0.088 mass of liquid to 1 mass of FM in composition FF6

by a 0.5-mm thick hard alumina disc. To minimise the amount of adsorbed water, all pieces were fired at high temperature (8 h at 1,000°C, then 24 h at 400°C for crushable MgO; 1 h at 600°C for NaCl; ≈24 h at 400°C for all other pieces), and then stored at 150°C. Just before an experiment, the full assemblage was fired a last time 24 h at 300°C. In all the experiments, the sample was placed at exactly the same height (to within 0.1 mm) into the graphite furnace to ensure good temperature reproducibility. Temperature was maximum at the bottom of the sample: ≈5°C larger than at the sample top and at the thermocouple tip. The reader is referred to Laporte et al. (2004) for more information on *P* and *T* monitoring.

To analyse the composition of liquids in equilibrium with mineral phases, we used the "microdike" technique developed by Laporte et al. (2004), which consists of extracting small volumes of liquid into fractures of the graphite container that formed during experiments. In all the experiments, we observed a few microdikes (Fig. 3a, b), both at the top and at the bottom of the sample chamber varying from tens to hundreds of microns in length and from a few microns to a few tens of microns in width. For large melt fractions and long run durations, as in our study, the liquid into the microdikes is in perfect equilibrium with the neighbouring mineral phases (Laporte et al. 2004). In a given experiment, the average glass compositions measured at the top and at the bottom are equal within error, as exemplified by sample FM1 in Table 3. The alkali contents (especially Na_2O) at the top tend to be slightly larger than at the bottom (but still whitin error); this result implies a slightly lower degree of melting at the top, which is in good agreement with the fact that the temperature at the top of the sample chamber is about 5°C lower than at the bottom.

Analytical techniques

At the end of an experiment, the capsule was enclosed in epoxy, sectioned lengthwise, polished and carbon-coated. Textures, phase assemblages and compositions (Tables 2, 3) were characterised using a JEOL JSM-5910 LV scanning electron microscope (SEM) and a Cameca SX100 electron microprobe. A 15-kV accelerating voltage, a 15-nA beam current, counting times of 10 s, and a focused beam were used for crystalline phases. For glass analyses, the beam current was lowered to 8 nA and a beam size of 5 μm was used whenever possible, otherwise 2 μm; sodium loss was negligible, even for glass analyses with a 2-μm beam size (Laporte et al., 2004). Relatively low analytical totals (between 93 and 96 wt%) were obtained in the case of very thin microdikes, due to beam overlap onto graphite. The proportions of liquid and solid phases best fitting the bulk composition of the starting material were calculated using a mass balance program modified from Albarède and Provost (1977).

Experimental results

In the presentation below, we do not follow the standard petrographic nomenclature, which places the boundary between lherzolite and harzburgite at 5% cpx and that

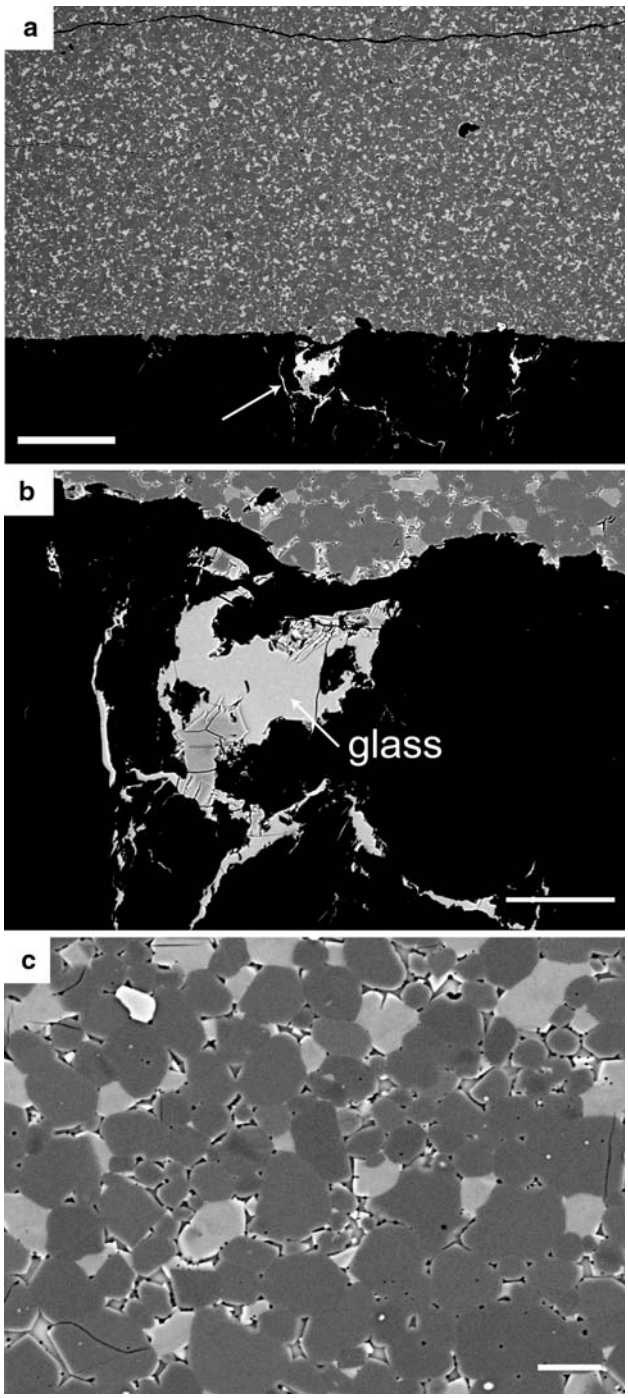

Fig. 3 Backscattered electron micrographs of a polished section of sample FM1. **a** An overall view of the lower part of the sample, showing the graphite container (*black*), the partially molten peridotite (*grey*), and a basaltic microdike (*arrow*). **b** Close-up view of the basaltic microdike showing a large pool of glass (*arrow*). **c** Close-up view of the partially molten peridotite showing a small fraction of interstitial melt (8.8 wt%) in equilibrium with ol (*grey*), opx (*slightly darker* than ol), cpx (*light grey*), and sp (*white*). Scales: 200 μm in **a**; 50 μm in **b**; 10 μm in **c**

between harzburgite and dunite at 10% opx + cpx. Following Asimow and Stolper (1999), we use instead the term harzburgite to refer to solid phase assemblages that are opx-bearing but cpx-free, and the term dunite for assemblages that are free of both opx and cpx.

Partial melting experiments of fertile mantle FM

Textures and phase equilibria

Four experiments were performed using composition FM as starting material (Table 2). The texture of sample FM1 (1.25 GPa-1,310°C) is shown in Fig. 3c; the textures of samples FM2 (1 GPa-1,290°C), FM3 (0.75 GPa-1,270°C) and FM4 (0.5 GPa-1,250°C) are shown in Fig. 4a–c. The grain size of the final products is significantly larger than the grain size of starting material (2–4 μm): indeed some ol grains exceed 30 μm in diameter. The melt fraction increases from 8.8 wt% at 1.25 GPa-1,310°C to 22.4 wt% at 0.5 GPa-1,250°C (Fig. 5a; Table 2). The ol fraction increases slightly with decreasing P and T that is with increasing melt fraction, while the fractions of opx, cpx, and sp decrease (Fig. 5b–d). Clinopyroxene is stable at 1.25 and 1 GPa (e.g., Fig. 3c); it is not stable in the 0.75 and 0.5 GPa experiments, in which it only occurs as quench overgrowths around opx. Accordingly, the solid assemblage changes from lherzolitic (ol + opx + cpx + sp) to harzburgitic (ol + opx + sp) somewhere between 1 and 0.75 GPa.

Liquid compositions

Average oxide concentrations in melts are shown in Fig. 6. With decreasing P and T, MgO decreases from 11.4 to 10.9 wt%, Na_2O from 2.8 to 1.6 wt%, FeO from 7.2 to 6.3 wt%, K_2O from 0.5 to 0.2 wt%, TiO_2 from 0.8 to 0.5 wt%, and Al_2O_3 from 16.8 to 15.8 wt%. The concentrations of Cr_2O_3 and SiO_2 increase from 0.1 and 49 wt% at 1.25 GPa-1,310°C, to 0.3 and 51.9 wt% at 0.5 GPa-1,250°C, respectively. The CaO content shows a concave downward pattern whose maximum value (12.3 wt% at 0.75 GPa) coincides with the disappearance of cpx.

Compositions of solid phases

A complete account of the compositions of solid phases is given in Table 3. Olivine, opx and cpx show little compositional variability within a single experimental charge. On the contrary, sp grains have more variable compositions, probably due to an incomplete equilibration of this phase. In any case, the variations observed within a single charge are negligible in comparison to the variations from one sample to another, even for sp: between 1.25 and 0.5 GPa, Ol-Mg# increases from 89.8 to 90.6, Opx-Mg# from 90.1 to 91.0, and Sp-Cr# from 15.6 to 48.6 (Table 3).

Table 3 Average compositions (wt%) of liquid and solid phases

Run no.	Phase	n[a]	SiO_2	TiO_2	Al_2O_3	Cr_2O_3	FeO*	MnO	MgO	CaO	Na_2O	K_2O	Total	Mg#[b]	Cr#[c]
FM															
FM1[d]	gl_{bottom}	12	49.01 (57)	0.84 (13)	16.80 (41)	0.12 (9)	7.17 (31)	0.14 (8)	11.35 (42)	11.27 (37)	2.81 (18)	0.50 (9)	97.93 (64)	73.83 (62)	–
	gl_{top}	3	48.62 (96)	0.94 (14)	17.08 (31)	0.08 (9)	7.15 (31)	0.16 (8)	11.37 (27)	11.01 (65)	3.04 (8)	0.54 (10)	95.87 (198)	73.94 (55)	–
	ol	11	40.72 (35)	0.02 (3)	0.09 (3)	0.11 (6)	9.82 (18)	0.15 (7)	48.63 (27)	0.30 (7)	–	–	99.77 (56)	89.8 (53)	–
	opx	8	53.62 (60)	0.12 (6)	6.28 (67)	0.91 (22)	6.00 (12)	0.14 (5)	30.59 (29)	2.27 (11)	–	–	99.99 (47)	90.09 (17)	–
	cpx	9	51.83 (42)	0.23 (6)	6.70 (33)	1.14 (12)	4.23 (28)	0.13 (8)	19.91 (45)	15.29 (68)	0.53 (6)	–	100.09 (52)	89.35 (54)	–
	sp	7	0.24 (5)	0.15 (5)	54.29 (200)	19.91 (223)	9.02 (33)	0.13 (7)	21.21 (63)	0.04 (4)	0.01 (3)	–	98.26 (53)	80.73 (103)	15.56 (245)
FM2	gl	6	49.83 (67)	0.66 (13)	16.47 (73)	0.16 (9)	7.00 (42)	0.16 (11)	11.33 (46)	12.08 (56)	2.00 (21)	0.30 (7)	94.73 (248)	74.26 (74)	–
	ol	8	40.51 (17)	0.01 (2)	0.08 (3)	0.16 (4)	9.60 (18)	0.14 (5)	49.00 (20)	0.32 (6)	–	–	100.61 (81)	90.10 (18)	–
	opx	5	54.80 (43)	0.07 (5)	4.05 (54)	0.94 (24)	5.85 (22)	0.16 (5)	31.67 (31)	2.36 (30)	–	–	100.99 (52)	90.62 (30)	–
	cpx	10	52.10 (49)	0.18 (5)	5.63 (41)	1.33 (17)	4.16 (31)	0.12 (6)	20.40 (129)	15.69 (154)	0.38 (11)	–	100.84 (68)	89.74 (24)	–
	sp	5	0.23 (5)	0.16 (5)	45.45 (338)	24.35 (315)	9.68 (49)	0.10 (8)	19.93 (33)	0.09 (5)	0.02 (3)	–	97.97 (122)	78.59 (109)	26.46 (396)
FM3	gl	10	51.10 (58)	0.58 (12)	16.04 (57)	0.20 (9)	6.48 (30)	0.11 (8)	11.14 (49)	12.29 (53)	1.82 (24)	0.23 (7)	98.18 (126)	75.40 (62)	–
	ol	15	40.65 (29)	0.02 (3)	0.06 (3)	0.21 (5)	9.31 (19)	0.15 (5)	49.20 (30)	0.33 (14)	–	–	100.44 (55)	90.42 (20)	–
	opx	5	55.09 (38)	0.07 (3)	3.60 (37)	1.10 (15)	5.73 (11)	0.13 (2)	31.75 (45)	2.49 (30)	–	–	100.59 (35)	90.80 (27)	–
	sp	4	0.19 (5)	0.18 (9)	35.22 (91)	35.20 (95)	10.46 (27)	0.18 (6)	18.46 (27)	0.10 (10)	0.00 (3)	–	97.39 (121)	75.87 (13)	40.13 (126)
FM4	gl	6	51.94 (93)	0.54 (17)	15.80 (60)	0.31 (9)	6.33 (73)	0.16 (12)	10.89 (92)	12.21 (58)	1.61 (66)	0.21 (8)	93.28 (439)	75.40 (56)	–
	ol	10	40.83 (22)	0.01 (3)	0.06 (2)	0.27 (7)	9.11 (23)	0.14 (6)	49.30 (35)	0.27 (3)	–	–	100.35 (64)	90.61 (25)	–
	opx	5	55.36 (78)	0.09 (8)	3.17 (113)	1.21 (26)	5.67 (14)	0.14 (5)	32.05 (79)	2.29 (24)	–	–	100.64 (60)	90.97 (24)	–
	sp	4	0.17 (11)	0.21 (6)	29.47 (115)	41.55 (133)	10.74 (29)	0.16 (6)	17.58 (45)	0.11 (5)	0.01 (3)	–	96.94 (75)	74.48 (75)	48.61 (174)
FF3															
FF3-3	gl	9	49.65 (63)	0.84 (12)	17.56 (37)	0.14 (8)	6.67 (43)	0.16 (11)	10.53 (31)	11.37 (23)	2.65 (10)	0.43 (7)	98.75 (95)	73.79 (43)	–
	ol	5	40.62 (34)	0.02 (5)	0.04 (5)	0.13 (5)	9.63 (8)	0.16 (4)	49.11 (16)	0.27 (3)	–	–	99.66 (33)	90.09 (4)	–
	opx	3	53.73 (75)	0.15 (4)	5.15 (66)	1.33 (53)	5.86 (7)	0.10 (4)	31.06 (99)	2.60 (76)	–	–	99.92 (32)	90.44 (17)	–
FF3-2	cpx	7	52.14 (42)	0.16 (8)	5.24 (56)	1.54 (26)	4.50 (40)	0.07 (8)	21.07 (89)	14.83 (130)	0.45 (9)	–	99.59 (71)	89.31 (59)	–
	sp	3	0.25 (5)	0.15 (5)	44.44 (41)	25.76 (67)	9.66 (27)	0.12 (6)	19.52 (27)	0.10 (5)	0.00 (3)	–	97.98 (13)	78.26 (18)	28.00 (71)
	gl	5	51.74 (86)	0.73 (6)	15.97 (52)	0.22 (9)	6.62 (12)	0.16 (6)	10.40 (95)	11.71 (61)	2.11 (11)	0.34 (6)	99.08 (169)	73.50 (160)	–
	ol	7	41.10 (29)	0.02 (5)	0.06 (3)	0.20 (11)	9.23 (20)	0.15 (10)	48.91 (32)	0.31 (4)	–	–	100.46 (43)	90.42 (22)	–
	opx	4	54.98 (63)	0.12 (3)	3.94 (102)	1.12 (46)	5.71 (8)	0.14 (3)	31.45 (88)	2.53 (9)	–	–	100.78 (52)	90.76 (25)	–
	sp	6	0.27 (8)	0.25 (6)	37.51 (111)	32.56 (107)	10.31 (32)	0.14 (5)	18.79 (26)	0.15 (3)	0.02 (4)	–	97.81 (69)	76.46 (75)	36.81 (144)
FF3-1	gl	7	53.41 (60)	0.64 (12)	15.96 (30)	0.31 (11)	5.92 (29)	0.11 (9)	10.00 (26)	11.32 (40)	1.98 (22)	0.34 (9)	99.11 (170)	75.07 (47)	–
	ol	7	40.85 (39)	0.02 (6)	0.05 (3)	0.31 (8)	9.27 (27)	0.14 (6)	49.06 (26)	0.29 (7)	–	–	100.51 (48)	90.42 (28)	
	opx	6	55.66 (52)	0.10 (5)	2.90 (78)	1.08 (24)	5.83 (28)	0.14 (6)	32.05 (69)	2.23 (69)	–	–	100.68 (96)	90.74 (44)	–
	sp	3	0.27 (7)	0.35 (6)	28.73 (112)	41.99 (105)	10.98 (40)	0.17 (5)	17.37 (27)	0.14 (13)	0.00 (3)	–	97.17 (138)	73.83 (87)	49.51 (158)

Table 3 continued

Run no.	Phase	n[a]	SiO_2	TiO_2	Al_2O_3	Cr_2O_3	FeO*	MnO	MgO	CaO	Na_2O	K_2O	Total	Mg#[b]	Cr#[c]
FF6															
FF6-3	gl	4	50.46 (39)	0.79 (13)	16.31 (54)	0.23 (21)	7.08 (41)	0.19 (24)	10.71 (66)	11.33 (38)	2.47 (12)	0.45 (4)	94.37 (51)	72.90 (209)	
	ol	4	40.59 (51)	0.01 (2)	0.10 (3)	0.24 (9)	9.49 (26)	0.16 (7)	49.09 (36)	0.32 (6)	–	–	99.99 (75)	90.22 (14)	–
	opx	4	53.87 (59)	0.14 (2)	5.31 (80)	1.16 (10)	5.77 (18)	0.16 (3)	31.06 (15)	2.51 (27)	–	–	100.19 (26)	90.57 (31)	–
	cpx	5	52.09 (26)	0.22 (4)	5.67 (67)	1.45 (10)	4.23 (18)	0.14 (7)	20.71 (26)	15.00 (85)	0.49 (11)	–	100.17 (41)	49.71 (39)	
	sp	5	0.22 (6)	0.23 (4)	43.51 (312)	26.42 (316)	9.68 (66)	0.15 (7)	19.63 (84)	0.13 (4)	0.01 (2)	–	98.02 (86)	78.33 (176)	28.99 (393)
FF6-2	gl	14	52.00 (41)	0.73 (9)	15.94 (19)	0.26 (6)	6.47 (21)	0.12 (4)	10.33 (35)	11.47 (26)	2.28 (16)	0.41 (5)	98.23 (234)	74 (125)	–
	ol	8	40.60 (39)	0.02 (5)	0.07 (5)	0.23 (8)	9.40 (28)	0.15 (6)	49.21 (26)	0.31 (6)	–	–	99.87 (19)	90.32 (25)	–
	opx	4	54.54 (66)	0.14 (4)	4.39 (41)	1.11 (66)	5.85 (21)	0.13 (6)	31.50 (125)	2.35 (94)	–	–	100.38 (82)	90.57 (18)	–
	cpx	5	51.93 (62)	0.37 (26)	5.77 (188)	1.29 (49)	3.99 (53)	0.13 (8)	19.37 (117)	16.73 (184)	0.43 (34)	–	100.47 (73)	89.67 (86)	–
	sp	6	0.21 (8)	0.28 (6)	40.11 (246)	30.13 (278)	9.96 (33)	0.16 (9)	18.98 (20)	0.17 (11)	0.01 (3)	–	97.42 (87)	68.82 (97)	33.51 (109)
FF6-1	gl	5	51.26 (59)	0.66 (6)	15.16 (50)	0.37 (6)	6.62 (35)	0.10 (6)	12.12 (58)	11.10 (60)	2.22 (20)	0.40 (15)	99.03 (108)	74.75 (102)	–
	ol	10	40.69 (39)	0.01 (2)	0.07 (3)	0.35 (7)	8.91 (25)	0.14 (6)	49.53 (36)	0.30 (9)	–	–	100.06 (52)	90.85 (24)	–

All compositions are normalised to a sum of 100% (original analytical totals are reported in the column "Total"). Glass compositions were analysed in microdikes using a 2-μm beam size (5 μm in runs FM-1, FF3-3 and FF3-1); the low analytical totals in FM-2, FM-4 and FF6-3 are due to beam overlap onto graphite. For a given phase in a given sample, we calculated the statistical dispersion of the data set (as measured by 2σ, where σ is the standard deviation) and the analytical error (following Ancey et al. 1978) and we selected the largest of these two values as an estimation of the error. The errors (in parentheses) are given in terms of least unit cited

[a] Number of analyses

[b] Mg# is the molar ratio 100 $Mg^{2+}/(Mg^{2+}+Fe^{2+})$; we considered that all iron was as Fe^{2+}

[c] Cr# is the molar ratio 100 $Cr^{3+}/(Cr^{3+}+Al^{3+})$

[d] Compositions of glasses analysed in microdikes at the bottom (gl_{bottom}) and at the top (gl_{top}) are given

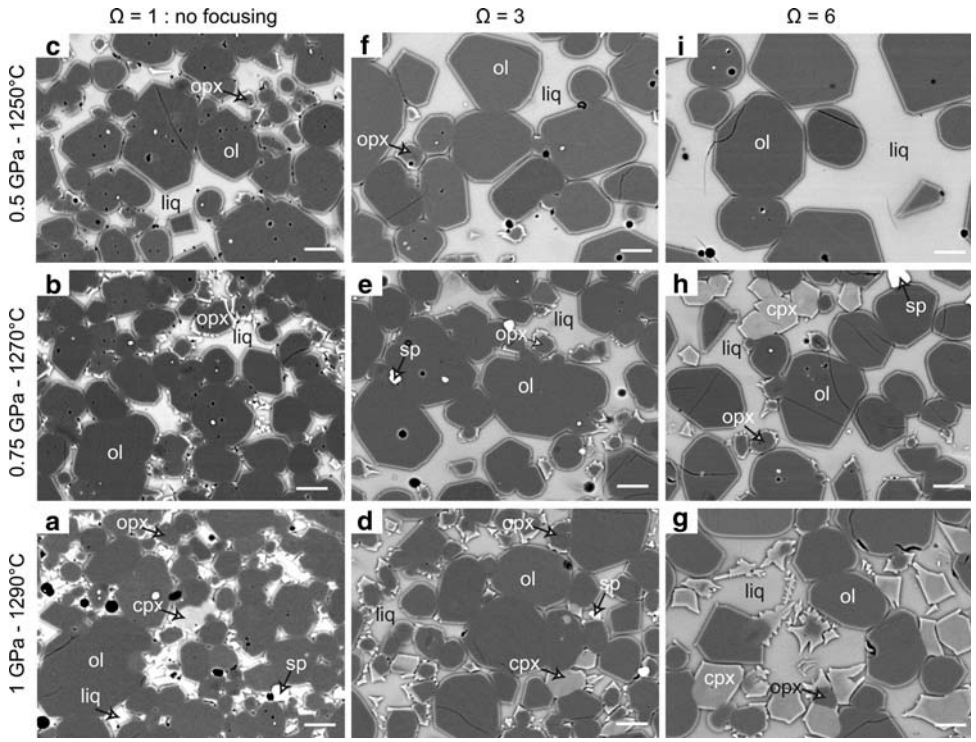

Fig. 4 Backscattered electron micrographs illustrating the textures and phase assemblages in the three experimental series. **a–c** Partial melting experiments of fertile mantle FM ($\Omega = 1$) at 1 GPa-1,290°C (**a**, FM2); 0.75 GPa-1,270°C (**b**, FM3); and 0.5 GPa-1,250°C (**c**, FM4). **d–f** Basalt–peridotite interaction experiments for $\Omega = 3$ (composition FF3), at 1 GPa-1,290°C (**d**, FF3-3); 0.75 GPa-1,270°C (**e**, FF3-2); and 0.5 GPa-1,250°C (**f**, FF3-1). **g–i** Basalt–peridotite interaction experiments for $\Omega = 6$ (composition FF6), at 1 GPa-1,290°C (**g**, FF6-3); 0.75 GPa-1,270°C (**h**, FF6-2); and 0.5 GPa-1,250°C (**i**, FF6-1). Note that the opx fraction decreases systematically with increasing Ω at 0.5 GPa (from 12.1% at $\Omega = 1$, to 1.2% at $\Omega = 3$, to 0% at $\Omega = 6$), and that liquid is in equilibrium with ol only in run FF6-1 (**i**). Scale bars: 10 μm

Series FF3: focusing factor $\Omega = 3$

Textures and phase equilibria

Three experiments were performed using composition FF3 as starting material (Table 2). The textures of samples FF3-3 (1 GPa-1,290°C), FF3-2 (0.75 GPa-1,270°C) and FF3-1 (0.5 GPa-1,250°C) are shown in Fig. 4d–f. The modes of the run products are given in Table 2, as well as the theoretical mode of composition FF3 at 1.25 GPa-1,310°C. The melt fraction increases from 26.5 wt% at 1 GPa-1,290°C to 36.4 wt% at 0.5 GPa-1,250°C (Fig. 5a). The fractions of ol, opx, and cpx are plotted as a function of melt fraction in Fig. 5b–d: with increasing melt fraction, the ol fraction increases from 53 to 62 wt%, while the fractions of all other solid phases (opx, cpx, and sp) decrease. The rate of decrease is specially fast in the case of opx, in comparison to partial melting experiments FM1-4 (Fig. 5c): opx fraction drops from 14 wt% at 1 GPa to only 1 wt% at 0.5 GPa. At 1 GPa, cpx is stable in addition to ol, opx, and sp, and the solid assemblage is lherzolitic. At 0.75 and 0.5 GPa, cpx is only stable as quench overgrowths, and the stable assemblage is harzburgitic (ol + opx + sp); there is, however, only 1.2 wt% opx for 62.1 wt% ol at 0.5 GPa, so that the solid residue is almost a dunite (Fig. 4f).

Liquid compositions

Oxide concentrations in glasses are plotted as a function of pressure in Fig. 6. The evolution of liquid compositions with decreasing P is the same as that observed in partial melting experiments FM1-4: (a) the concentrations in MgO, Al_2O_3, Na_2O, FeO, K_2O and TiO_2 decrease; (b) the concentrations in SiO_2 and Cr_2O_3 increase; and (c) the CaO content shows a concave downward pattern with a maximum (11.7 wt% at 0.75 GPa) coinciding with cpx exhaustion. The trends of liquid compositions in series FF3 may be extended to 1.25 GPa-1,310°C by noting that, just after the focusing event, the melt composition is theoretically the same as in partial melting experiment FM1. For all oxides except Al_2O_3, the data points at 1.25 GPa-1,310°C fit well into the trends defined by liquids in series FF3. The Al_2O_3 content at 1.25 GPa does not fit into the trend of decreasing alumina content with decreasing pressure, although it is nearly equal within error to the Al_2O_3

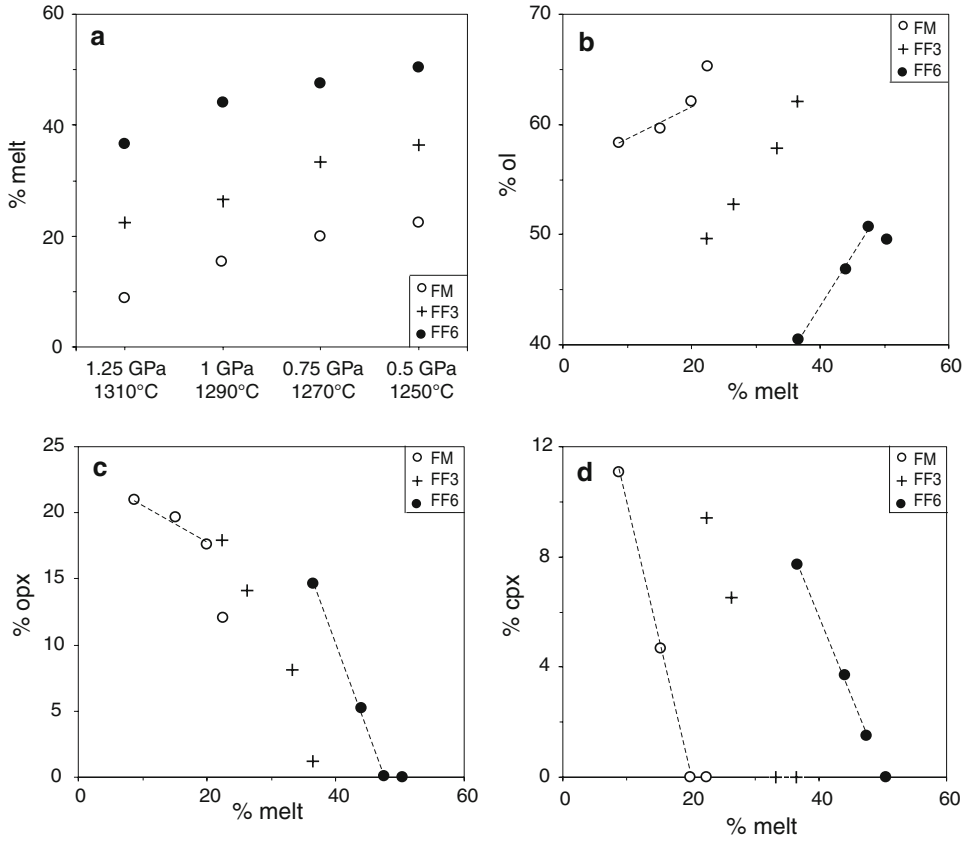

Fig. 5 **a** Plot of melt percentage as a function of *P* and *T*. **b–d** Weight percentages of ol (**b**), opx (**c**), and cpx (**d**) plotted as a function of melt percentage; the *dashed lines* are the best fit lines used to compute the coefficients of the melting reactions. Symbols are as follows: *empty circles* FM series, *crosses* FF3 series, *solid circles* FF6 series. The uncertainties on phase percentages are given in Table 2

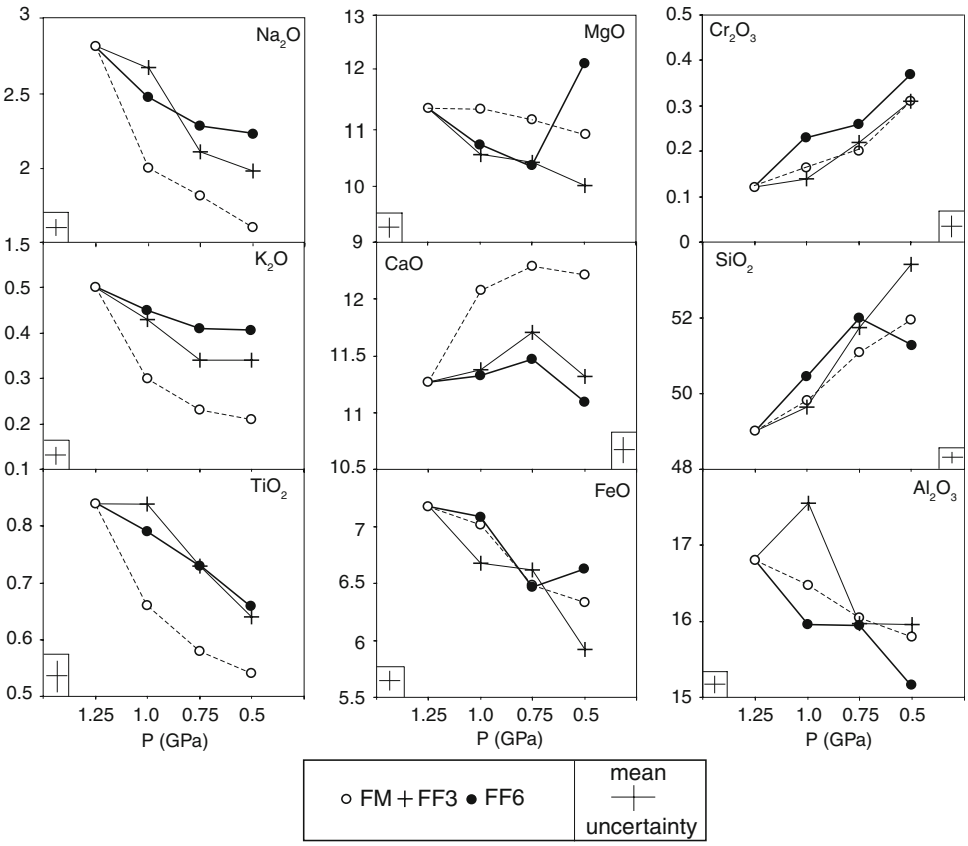

Fig. 6 Evolution of glass compositions (in wt%) as a function of pressure. Symbols are as follows: *empty circles* FM series, *crosses* FF3 series, *solid circles* FF6 series. *Error bar* on oxide concentrations are 1σ standard deviations on average glass analyses. Uncertainties in pressure are estimated to be ± 0.05 GPa

content at 1.0 GPa (16.8 ± 0.4 wt% at 1.25 GPa vs. 17.5 ± 0.4 wt% at 1 GPa; Table 3).

Compositions of solid phases

All solid phases are relatively homogeneous in a given sample. Ol-Mg# and Opx-Mg# show only very faint variations with decreasing *P*; for instance, Ol-Mg# increases from 89.8 at 1.25 GPa to 90.1 at 1.0 GPa and 90.4 at 0.5 GPa (Table 3). On the contrary, the compositional variation of sp is much larger: Sp-Cr# increases from 15.6 at 1.25 GPa to 28.0 at 1.0 GPa and 49.5 at 0.5 GPa.

Series FF6: focusing factor $\Omega = 6$

Textures and phase equilibria

Three experiments were performed using composition FF6 as starting material (Table 2). The textures of samples FF6-3 (1 GPa-1,290°C), FF6-2 (0.75 GPa-1,270°C) and FF6-1 (0.5 GPa-1,250°C) are shown in Fig. 4g–i. The modes of the run products and the theoretical mode of composition FF6 at 1.25 GPa-1,310°C are given in Table 2. The three experiments of series FF6 are characterised by large melt fractions and mean grain sizes in comparison to partial melting experiments FM1-4. In terms of phase stability and mode, the main points may be summarised as follows (Fig. 5; Table 2): (a) the liquid fraction increases very regularly with decreasing *P* and *T*, from 36.7 wt% up to 51 wt%; (b) the ol fraction increases from 40.5 wt% at 1.25 GPa-1,310°C to 50.7 wt% at 0.75 GPa-1,270°C; but then it decreases to 49 wt% at 0.5 GPa-1,250°C; (c) opx is only stable down to 0.75 GPa, and, at a given *P*, its modal percentage (14.6 wt% at 1.25 GPa, only 0.1 wt% at 0.75 GPa) is lower than in the two previous series of experiments; and (d) the cpx fraction decreases relatively slowly with decreasing *P* so that cpx is still present at 0.75 GPa, whereas it is only stable down to 1 GPa in compositions FM and FF3; and (e) sp is not stable at 0.5 GPa. Accordingly, two types of phase assemblage may be distinguished as a function of pressure:

1. At 1.0 and 0.75 GPa, the equilibrium phase assemblage is ol + opx + cpx + sp + liquid. Unlike all lherzolitic phase assemblages reported so far, in which opx is more abundant than cpx, the cpx fraction is larger than the opx fraction in experiments FF6-3 and FF6-2.
2. At 0.5 GPa, the equilibrium phase assemblage is ol + liquid, and the solid residue is a dunite.

The transition from a lherzolitic assemblage to a dunitic one is accompanied by a major change in the melting reaction, as shown by the evolution of the ol fraction in Fig. 5b: at $P \geq 0.75$ GPa, ol is on the product side of the melting reaction and its fraction increases with decreasing *P*; below 0.75 GPa, ol is consumed in the melting reaction and its fraction decreases from 50.7 wt% at 0.75 GPa to 49 wt% at 0.5 GPa.

Liquid compositions

Oxide concentrations in melts are shown in Fig. 6. For most elements, the evolution with decreasing pressure (and thus increasing melt fraction) is similar to that reported for compositions FM and FF3: in particular, Al_2O_3, K_2O, Na_2O, and TiO_2 decrease, and Cr_2O_3 increases. On the contrary, SiO_2 and MgO show very different patterns due to the fact that ol switches from a reaction product to a reactant between 0.75 and 0.5 GPa. Silica first increases up to 52.0 wt% at 0.75 GPa, then it decreases to 51.3 wt% at 0.5 GPa. MgO shows a symmetrical pattern; it first decreases down to 10.3 wt% at 1.0 and 0.75 GPa, then it increases to 12.1 wt% due to the dissolution of olivine into the liquid.

Compositions of solid phases

The main changes in mineral chemistry between 1.25 and 0.75 GPa are a strong increase of Cr# in sp and slight increases of Mg# in ol and opx (Table 3). Unlike series FF3, Ol-Mg# increases markedly between 0.75 and 0.5 GPa (from 90.3 to 90.9), in relation to the transition from a lherzolitic to a dunitic solid residue.

pMELTS calculations

Theoretical approach

In order to extrapolate our data to larger focusing factors, we used the algorithm pMELTS (Ghiorso and Sack 1995; Asimow et al. 2001; Ghiorso et al. 2002) to calculate the equilibrium phase assemblages in a set of compositions covering a range of focusing factors from 1 to 23 at different *P* and *T*. This set comprised the three compositions used as starting materials in our experiments (FM, FF3, and FF6, for $\Omega = 1$, 3, and 6, respectively), and five additional compositions FF4 ($\Omega = 4$), FF7 ($\Omega = 7$), FF11 ($\Omega = 11$), FF21 ($\Omega = 21$) and FF23 ($\Omega = 23$). A major advantage of pMELTS in comparison to the experimental approach is that it allows to evaluate rapidly the effect of the main parameters (*P*-*T*, Ω) on phase proportions and compositions. Despite periodic improvements, however, pMELTS still suffers a few important limitations. In the case of mantle melting, there are two main limitations: (a) the program underestimates the melt fraction at a given temperature; and (b) in the presence of Cr_2O_3, sp remains stable at temperatures much larger than the experimental stability limit.

In practice, we used the isobaric mode of the program to fully characterise the assemblage (paragenesis, modes and phase compositions) in a given bulk composition, at fixed P and T ranging from the liquidus to the solidus. The calculations were made in three steps. We first entered the bulk composition of system, the pressure and the oxygen fugacity. In the mantle beneath mid-ocean ridges as well as in our experiments, f_{O_2} lies somewhere between FMQ-1 and FMQ-2 (where FMQ stands for the buffer fayalite-magnetite-quartz; Christie et al. 1986; Laporte et al. 2004). Our calculations were made at FMQ-1; for comparison, we also performed a few calculations at FMQ-2, and we obtained similar results. The second step consisted in computing phase proportions and compositions over a range of temperatures, from the liquidus to the solidus temperature. Finally, in the third step, we compared pMELTS predictions for $\Omega = 1$, 3, and 6 to our experimental results for bulk compositions FM, FF3, and FF6. As the program underestimates the melt fraction at a given temperature, these comparisons were not made on the basis of temperature, but on the basis of melt fraction. The most representative results are reported in Table 4.

Partial melting of fertile mantle composition FM

Phase proportions

For composition FM at pressures and melt fractions similar to the experimental ones, pMELTS calculates the same assemblages as in runs FM1-4: lherzolitic at 1.25 and 1.0 GPa, harzburgitic at 0.75 and 0.5 GPa (Fig. 7).

Liquid compositions

Oxide concentrations in experimental and theoretical melts are plotted as a function of melt fraction in Fig. 7. In the case of K_2O, Na_2O and TiO_2, predicted melt compositions match well the compositions analysed in our samples. The exaggerated stability of spinel in pMELTS calculations leads to underestimated Cr_2O_3 and Al_2O_3 concentrations in melts. For the other oxides, the theoretical trends are qualitatively in good agreement with the experimental trends, albeit systematically steeper.

Theoretical constraints on the effects of magma focusing

The calculations were made for $\Omega = 3$, 4, 6, 11, and 21, $P = 0.5$ GPa, and a range of temperatures from the liquidus to the solidus. For $\Omega = 3$ and 6, we finally selected the temperature that yielded a melt fraction equal to the melt fraction in experiments FF3-1 and FF6-1 (36.4 and 51 wt%, respectively): 1,290°C for $\Omega = 3$, and 1,294°C for $\Omega = 6$, as compared to an experimental temperature of 1,250°C (Table 4). As we had no experimental constraint to select temperature for $\Omega = 4$, 11 and 21, we fixed T at 1,294°C as for $\Omega = 6$.

Phase proportions

At $P = 0.5$ GPa, pMELTS predicts the solid phase assemblages ol + opx + sp for $\Omega = 3$, and ol + sp for $\Omega \geq 4$. These predictions are in good agreement with our experiments, as the solid residue was harzburgitic in sample FF3-1, and dunitic in sample FF6-1 (Fig. 7). We did not observe sp in run FF6-1; the presence of sp in the calculated phase assemblages for $\Omega \geq 6$ is presumably due to an incorrect partitioning of Cr_2O_3 between sp and liquid in pMELTS.

Liquid compositions

Oxide concentrations in experimental and theoretical melts at $P = 0.5$ GPa and Ω ranging from 1 to 21 are plotted as a function of melt fraction in Fig. 7. In the case of K_2O, Na_2O and TiO_2, the agreement between predicted melt compositions and the compositions measured in runs FM4, FF3-1, and FF6-1 is perfect. This agreement is mainly due to the fact that we compare theoretical and experimental results at a given melt fraction. The agreement is also perfect in the case of CaO while the agreement between the CaO concentrations computed for composition FM at $P \geq 1$ GPa and the concentrations measured in runs FM1-2 was not good. This means that pMELTS provides reliable estimates of the CaO concentrations in liquid when cpx is not stable. At $\Omega = 3$, the MgO and FeO contents in the liquid are underestimated and the SiO_2 content is overestimated because the opx fraction computed by pMELTS is too low and the ol fraction too large. For these three elements, the agreement between the calculated concentrations and the measured ones is much better at $\Omega = 6$ because opx is no longer stable. At all values of Ω, pMELTS yields very poor estimates of the Cr_2O_3 contents in the liquid. At last, FeO and CaO increase and SiO_2 and MgO decrease at high values of Ω ($\Omega \geq 11$). For these high values of Ω, the evolution of melt composition seems to be controlled by a dilution effect by the liquid added to the system at the focusing level. A discussion and a detailed analysis of the evolution of melt composition as a function of Ω will be presented below.

Focusing factors required to produce dunites at high pressure

A fundamental parameter in focused magma ascent is the pressure, hereafter referred to as P_{Dunite}, at which pyroxenes are exhausted from the solid residue and below which the liquid is in equilibrium with ol (±sp) only.

Table 4 Most representative results of pMELTS calculations

	P (GPa)	T (°C)	Ω[a]	Phase proportions (wt%)					Liquid compositions (wt%)										Ol-Mg#[d]	Sp-Cr#[d]
				Liq	Ol	Opx	Cpx	Sp	SiO_2	TiO_2	Al_2O_3	Cr_2O_3	FeO[b]	MgO	CaO	Na_2O	K_2O	Mg#[c]		
FM																				
FM-1	1.25	1,372	1	8.8	56.6	20.8	11.3	2.6	48.59	0.77	15.93	0.09	7.58	13.44	9.85	3.28	0.45	76.0	90.2	19.9
FM-2	1	1,351		15.4	59.5	17.9	5.4	1.9	50.12	0.66	15.71	0.10	6.94	12.74	11.32	2.14	0.26	76.6	90.5	27.3
FM-3	0.75	1,322		20.0	65.9	12.7	Absent	1.3	52.55	0.57	15.15	0.12	6.06	11.64	12.12	1.57	0.18	77.4	90.7	41.3
FM-4	0.5	1,283		22.4	69.9	6.5	Absent	1.1	55.33	0.55	15.36	0.12	5.05	10.02	11.92	1.47	0.17	78.0	90.7	52.1
FF																				
FF-23	1	1,344	**23**	76.0	23.4	Absent	Absent	0.6	49.64	0.81	15.83	0.11	6.87	12.02	11.46	2.77	0.46	75.7	90.2	27.4
FF-7	0.75	1,307	**7**	50.8	48.3	Absent	Absent	0.9	52.00	0.76	15.84	0.13	6.00	10.63	11.73	2.50	0.40	76.0	90.2	36.28
FF-3	0.5	1,290	3	36.4	62.5	0.2	Absent	0.9	55.47	0.70	16.27	0.16	4.53	9.00	11.39	2.17	0.31	78.0	90.3	47.2
FF-4		1,294	**4**	41.2	57.9	Absent	Absent	0.8	54.12	0.70	16.13	0.16	5.03	10.20	11.22	2.25	0.35	78.3	90.3	45.6
FF-6		1,294	6	50.6	48.7	Absent	Absent	0.7	51.54	0.70	15.16	0.19	6.54	12.12	11.10	2.29	0.36	76.8	90.1	41.6
FF-11		1,294	11	62.5	37.0	Absent	Absent	0.6	50.35	0.76	15.56	0.19	6.79	12.12	11.24	2.55	0.41	76.1	89.9	34.6
FF-21		1,294	21	75.1	24.6	Absent	Absent	0.4	49.48	0.80	15.87	0.18	6.98	12.14	11.34	2.73	0.45	75.6	89.7	30.5

The bulk compositions used in the calculations are given in the first column. Two sets of data are reported: (a) decompression melting of fertile mantle FM from 1.25 GPa to 0.5 GPa; and (b) basalt-peridotite interaction at $P = 1$, 0.75 and 0.5 GPa and for various values of Ω

[a] Bold values of Ω are the required values to produce a dunitic residue at 1, 0.75 and 0.5 GPa

[b] all iron is considered as Fe^{2+}

[c] Mg# = 100 $Mg^{2+}/(Mg^{2+}+Fe^{2+})$ in the liquid phase, where all iron is as Fe^{2+}

[d] Compositions of solid phases are indicated by the Ol-Mg# and by the Sp-Mg#

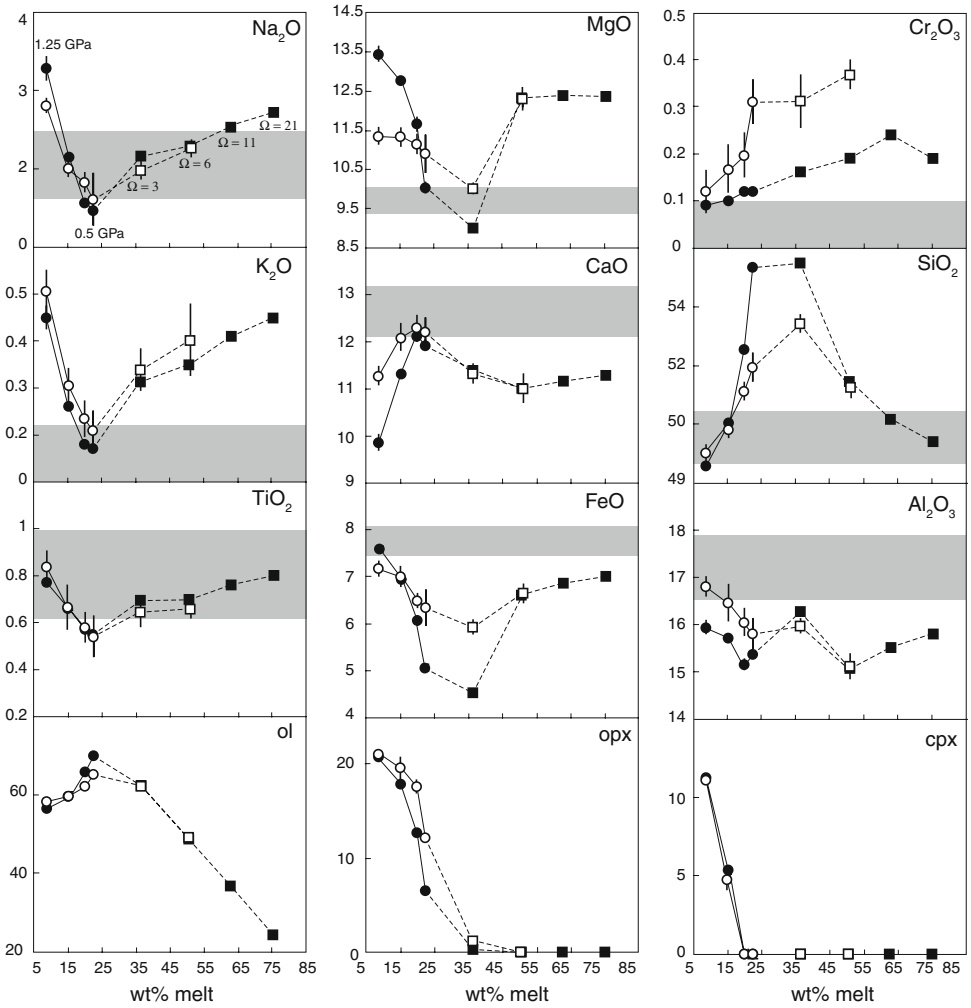

Fig. 7 Comparison of liquid compositions and weight percentages of ol, opx and cpx in our experiments with the compositions and modes calculated using pMELTS (oxide concentrations and modes in wt% are plotted as function of melt fraction). Two sets of data are compared: (1) decompression melting of fertile mantle FM at 1.25 GPa-1,310°C; 1GPa-1,290°C; 0.75 GPa-1,270°C; 0.5 GPa-1,250°C; and (2) basalt-peridotite interaction at $P = 0.5$ GPa and $\Omega = 3$, 6, 11, and 21 (see the labels on the Na_2O plot). Symbols are as follows: *circles* for decompression melting, *squares* for basalt-peridotite interaction, *empty symbols* for experimental data, and *solid symbols* for theoretical data. When not visible, the error bar (1σ) is smaller than the symbol. The range of primitive MORB compositions (see Fig. 1) is indicated by the *shaded boxes*

Calculations were made to evaluate the values of Ω required to produce dunites at pressures equal to 0.5, 0.75, and 1 GPa. By analogy with calculations at 0.5 GPa, we selected the temperatures that yielded a melt fraction equal to that in experiment FF6-2 for the 0.75 GPa models, and to that in experiment FF6-3 for the 1 GPa models namely, 1,307°C at 0.75 GPa and 1,344°C at 1 GPa. Focusing factors of 4, 7, and 23 are required to yield $P_{\text{Dunite}} = 0.5$, 0.75 and 1 GPa, respectively (Table 4). Considering that the melt fraction f in fertile mantle FM at the focusing level is 0.088, these focusing factors correspond to magma/rock ratios $(\Omega - 1)f$ equal to 0.26, 0.52, and 1.94.

Discussion and petrologic implications

Limitations of this study

Experimental limitations

In our simplified model, we supposed that, after the focusing event at 1.25 GPa, the system is closed and only undergoes decompression melting down to 0.5 GPa (step no. 3 in Fig. 2). Accordingly, the experiments do not reproduce a fundamental aspect of focused magma transport; the fast ascent of liquid relative to the solid matrix into highly permeable channels. Also, a single focusing event is an oversimplification. In nature, focusing is presumably a continuous process, or it involves a succession of discrete events. Hart (1993) envisioned a branching network of highly permeable channels with a lot of small channels in depth, whose confluence gives rise to fewer and fewer, and larger and larger channels upwards. According to Asimow and Stolper (1999), this scenario is more effective with respect to the generation of dunites and the chemical processing of ascending magmas.

Despite these limitations, our experiments reproduce in the laboratory the reaction between liquids produced in the deeper part of the melting column and peridotite at low to intermediate pressure. This allows us to evaluate the effect of *P-T*, and magma/rock ratio on the reaction products, and, specially, to constrain the conditions required to produce primitive MORB-like liquids in equilibrium with ol ± sp. Similar experiments have been performed in the

past (e.g., Kogiso et al. 1998; Yaxley 2000), but they applied to intraplate settings, not to mid-ocean ridges.

Theoretical limitations

Figure 7 shows some discrepancies between experimental results and pMELTS calculations, except for Na_2O, K_2O and TiO_2, for which experimental and theoretical melts are always in perfect agreement whatever the conditions (P, F, Ω). The exaggerated stability of spinel in pMELTS calculations leads to underestimated Cr_2O_3 concentration in melts, conditions (P, Ω) aside. In the case of CaO, there is a poor agreement between predicted melt compositions for fertile mantle FM at $P \geq 1$ GPa and the concentrations measured in runs FM1-2. These conditions correspond to an assemblage where cpx is stable. The accord is also weak in the case of SiO_2, MgO and FeO as long as opx is stable in the assemblage (FM1-4 and FF3-1). On the contrary, when opx and cpx are not stable, predicted melt compositions agree perfectly with the measured compositions (Fig. 7). This means that pMELTS provides reliable estimates of CaO, MgO, FeO and SiO_2 contents in the case of liquids in equilibrium with ol (+sp). In addition, pMELTS predicts that focusing factor necessary to produce a dunite at 0.5 GPa is equal to 4, in perfect agreement with our experimental brackets ($3 < \Omega < 6$). Accordingly, we can rely on pMELTS to compute the magma-rock ratio required to produce a dunitic residue and the melt compositions in equilibrium with this residue.

Basalt-peridotite interactions: the solid side

Magma/rock ratios required to produce dunites

It has been proposed that most dunite bodies in mantle peridotites result from the interactions between ascending basalts and host peridotites (e.g., Kelemen et al. 1997). Our experiments confirm that dunites can be produced by such a process, and show that relatively low magma/rock ratios are required to dissolve all pyroxenes of a fertile peridotite composition. Indeed, for $\Omega = 6$, that is for a magma/rock ratio $(\Omega - 1)f = 0.44$, the residual assemblage changes from ol + opx + cpx + sp at 0.75 GPa to ol only at 0.5 GPa (runs FF6-2 and FF6-1, respectively). The Ol-Mg# in sample FF6-1 is equal to 90.9, thus just slightly larger than the values expected in the case of simple partial melting of a fertile mantle composition (from 89.8 to 90.6 in our experiments FM1-4). This observation is in good agreement with the numerical model of Asimow and Stolper (1999) and with the geological studies of Kelemen et al. (1995) and Suhr et al. (2003), in which dunites are characterised by values of Ol-Mg# in the range 90.8–91.9.

Primitive MORBs are not saturated with opx except at pressures greater than about 0.8 GPa (O'Hara 1968; Elthon and Scarfe 1980; Stolper 1980; Elthon 1989). A possible explanation for this observation is that their parental melts migrated via highly permeable channels into which the transition from a pyroxene-bearing residue to a dunite residue occurred at pressures $\geq$0.8 GPa. In this context, it is important to be able to constrain the magma/rock ratios that are required to exhaust opx (and cpx) from the residue at a pressure of about 0.8 GPa. Our experiments and pMELTS calculations indicate that a focusing factor of 8—that is, a magma/rock ratio of $\approx$0.62—allows to generate dunites at $\approx$0.8 GPa: (a) in our experiments at $\Omega = 6$, the percentages of pyroxenes at 0.75 GPa are indeed very low (0.1 wt% opx, 1.5 wt% cpx; Table 2), implying that P_{Dunite} is close to 0.7 GPa; and (b) according to pMELTS, P_{Dunite} equals 0.75 GPa when the focusing factor is equal to 7. The calculations also show that the value of Ω required to produce dunites increases non-linearly with increasing P_{Dunite} from $\Omega = 4$ for $P_{\text{Dunite}} = 0.5$ GPa, to $\Omega = 7$ for $P_{\text{Dunite}} = 0.75$ GPa, and to $\Omega = 23$ for $P_{\text{Dunite}} = 1$ GPa (Table 4). Such a non-linear increase was also documented by Asimow and Stolper (1999), and can be qualitatively explained by the increase in opx stability relative to ol with increasing pressure (Yoder 1976; Elthon and Scarfe 1984). These calculations show that it is much easier to produce dunites at low pressure than at high pressure, because it requires much smaller magma/rock ratios. Note, however, that pMELTS tends to overestimate the stability of opx (Asimow and Stolper 1999), and so it probably overstates the difficulty of making dunite at high pressure.

Effect of the focusing factor on the melting reaction and on the modal composition of solid residues

The coefficients of the melting reaction can be computed from the slope of the experimental trends in plots of the weight fraction of crystalline phases as a function of melt fraction (Fig. 5b–d; see Baker and Stolper 1994). The trends in Fig. 5b–d show important variations of slopes depending on the focusing factor, suggesting that the coefficients of the melting reaction change significantly due to magma focusing. To illustrate this point, we computed the melting reaction in the cpx stability field in compositions FM and FF6. The melting reaction in composition FM consumes opx, cpx, and sp to produce liquid +ol, in the following proportions:

$$0.30(6)\text{opx} + 0.99(0)\text{cpx} + 0.04(0)\text{sp} = 1\,\text{liquid} + 0.32(7)\text{ol}$$

This reaction is close to that reported by Baker and Stolper (1994), except that the coefficients for cpx and ol

are a little bit larger. Note that their reaction corresponds to the case of isobaric (1 GPa) melting, whereas our reaction is for decompression melting: melting proceeds at increasing T in the former case, and at slightly decreasing T in the latter case. With the disappearance of cpx below 0.75 GPa, the melting reaction switches to opx + sp = liquid + ol, and the coefficients for opx and ol increase significantly, as indicated by the strong decrease of the opx fraction and increase of the ol fraction between 0.75 and 0.5 GPa (Fig. 5b, c).

Over the pressure range 1.25–0.75 GPa, the melting reaction in composition FF6 is

$$1.32(5)\text{opx} + 0.57(3)\text{cpx} + 0.03(3)\text{sp} = 1\ \text{liquid} + 0.93(7)\text{ol}$$

Accordingly, decompression melting in composition FF6 consumes much more opx and less cpx, and hence produces much more ol (Daines and Kohlstedt 1994; Braun 2004) than in mantle peridotite FM. This observation is consistent with numerical results of Asimow and Stolper (1999), which showed a progressive change of the stoichiometry of the melting reaction with increasing focusing: the mass of opx melted for a given melt fraction increases with Ω. This major effect of the focusing factor on the melting reaction is well illustrated by the changes in slopes of ol, opx, and cpx fractions as a function of Ω in Fig. 5b–d. At a pressure slightly lower than 0.75 GPa, the melting reaction in composition FF6 switches to ol → liquid, and the ol fraction starts decreasing.

The changes of the coefficients of the melting reaction with increasing Ω have strong implications for the modal composition of the residual solid. In compositions FM and FF3, the ratio opx/cpx in the residue is always >1, and increases with the degree of melting: in the FM series, for instance, it ranges from 1.9 at 1.25 GPa, to 4.2 at 1 GPa (the residue is cpx-free at lower pressure; Table 2). On the contrary, the opx/cpx ratio in composition FF6 decreases with increasing melt fraction, and drops below 1; it is equal to 1.4 at 1 GPa, and to 0.07 at 0.75 GPa. Accordingly, it is possible to produce residues with cpx > opx, or even residues with a small fraction of cpx but no opx, at high focusing factors.

Basalt-peridotite interactions: effects on the bulk chemical composition of the solid matrix

In our experiments, the modal percentage of ol in the residue ranges from 64 wt% in run FM1 to 100% in run FF6-1, resulting in an increase of the bulk MgO content of the solid matrix from about 41 wt% to more than 49 wt%. The bulk CaO, FeO, Al_2O_3, and SiO_2 contents of the solid (lherzolite and harzburgite) residues are plotted as a function of the bulk MgO content in Fig. 8. With increasing MgO, CaO decreases from 2.6 to 0.3 wt%, Al_2O_3 from 2.8 to 0.2 wt%, and SiO_2 from 44.7 to 40.7 wt%, and FeO increases slightly from 8.3 to 9.2 wt%. In comparison to partial melting in a closed system, basalt-peridotite interactions yield solid residues strongly enriched in olivine and MgO, and thus strongly depleted in CaO and Al_2O_3. In addition, the trends of decreasing SiO_2 and of increasing FeO are much steeper in the case of magma focusing (Ω increasing at fixed P and T) than in the case of closed-system partial melting, due to enhanced pyroxene dissolution. As a result, basalt-peridotite interactions may lead to solid residues significantly depleted in SiO_2 and enriched in FeO: for instance, the bulk solid contains ≈2 wt% less SiO_2 and ≈0.7 wt% more FeO in series FF6 than in series FM, at fixed MgO (Fig. 8).

Whole-rock compositions of ophiolitic peridotites from the Erro-Tobbio Unit (ET peridotites, Voltri Massif, Ligurian Alps; Rampone et al. 2004) and abyssal peridotites (Niu et al. 1997; Baker and Beckett 1999) are also plotted in Fig. 8. These data display positive FeO_{tot}–MgO, and negative SiO_2–MgO, Al_2O_3–MgO and CaO–MgO trends that are consistent with our experimental trends. The abyssal peridotite samples overlap both the basalt-peridotite interaction data and the partial melting data, but the compositions strongly depleted in CaO, Al_2O_3, and SiO_2 found in abyssal peridotites seem to bear the chemical signature of basalt-peridotite interactions. In fact, Niu and coworkers (Niu 1997; Niu et al. 1997) showed that abyssal peridotites display chemical features that are not consistent with various partial melting trends (polybaric near-fractional or isobaric batch melting). Moreover, according to Rampone et al. (2004), the ET peridotites cannot be interpreted as resulting from progressive partial melting, because constituent minerals from these peridotites have homogenous composition. Similar features observed in abyssal and ophiolitic peridotites by Kelemen et al. (1997) have been interpreted as the result of melt-peridotite reaction processes (e.g., Kelemen et al. 1995; Godard et al. 1995). In addition, the depleted ET peridotites exhibit nearly constant bulk-rock Mg#'s with increasing ol percentage (Fig. 9). Again, this observation is consistent with our experimental results: in our three series, the bulk Mg# of the solid residues (harzburgite and lherzolite) increases with increasing ol percentage, but the rate of increase is larger in the case of partial melting than in the case of basalt-peridotite interaction. In general, it is likely that the bulk chemical composition of the solid matrix is controlled by a combination of these two processes, partial melting and basalt-peridotite interaction: initially the mantle

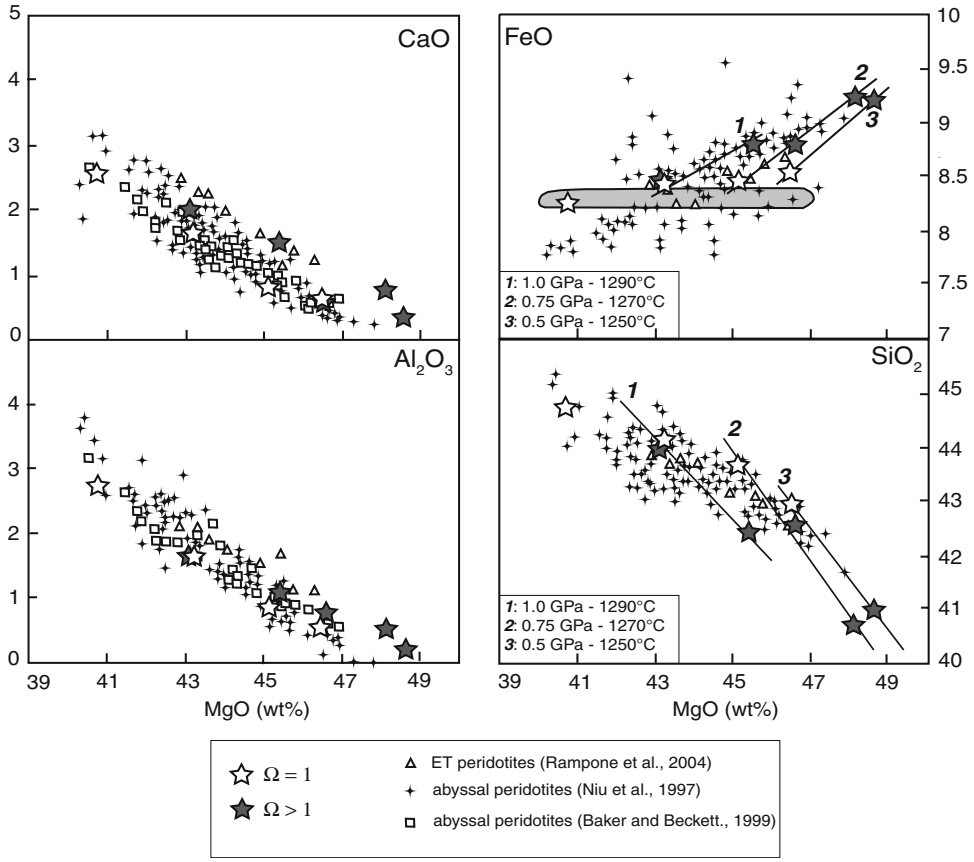

Fig. 8 Abundances of CaO, Al_2O_3, SiO_2 and FeO_{tot} versus MgO in the lherzolite and harzbugite residues of our experiments (*empty stars* partial melting experiments, *solid stars* basalt–peridotite interaction experiments) compared with the compositions of Erro-Tobbio (ET) peridotites (*empty triangles*, Rampone et al. 2004) and estimated compositions of abyssal peridotites (*crosses* data from Niu et al. 1997; *empty squares* or *shaded field* data from Baker and Beckett 1999). In the SiO_2 versus MgO and FeO versus MgO diagrams, the experimental data corresponding to same values of *P* and *T* and different focusing factors ($\Omega = 1$, 3, and 6) are fitted by straight lines labelled 1 (1 GPa-1,290°C), 2 (0.75-1,270°C), and 3 (0.5 GPa-1,250°C) (Sample FF6-1 is not plotted in this figure as it corresponds to a dunitic residue)

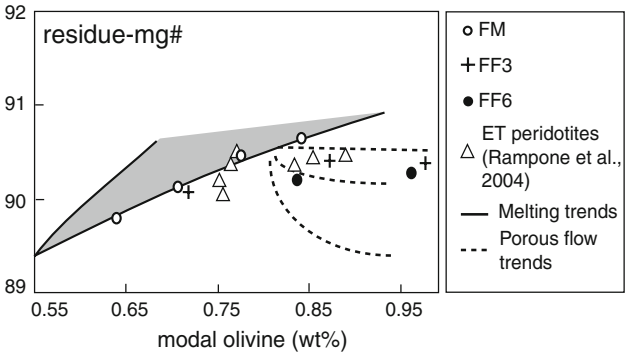

Fig. 9 Bulk magnesium number of the residue, as a function of the mass fraction of olivine in lherzolite and harzburgite residues from our experiments, and in peridotites from the Erro-Tobbio unit (Rampone et al. 2004). Symbols are as follows: *empty circles* FM series, *crosses* FF3 series, *solid circles* FF6 series, *empty triangles* Erro-Tobio peridotites. The *shaded field* shows the correlations between Mg# and olivine mass fraction in solid residues produced by partial melting, assuming different melting reactions in the spinel stability field (from Bedini et al. 2002). The *dashed lines* are trends computed assuming a reactive porous flow process, involving olivine crystallisation and pyroxene dissolution (the three lines correspond to three different compositions of percolating melt; from Bedini et al. 2002)

probably undergoes partial melting and the residue reflects this dominantly; as upwelling continues, more melts are produced and basalt-peridotite interactions are prevalent.

Basalt-peridotite interactions: the liquid side

Primitive MORB compositions versus partial melts of peridotites

The liquid compositions analysed in partial melting experiments FM1-4 are plotted in the two ternary projections of Fig. 10. The compositions computed in the case of batch melting of a mantle source at 1.5 and 1.0 GPa using Kinzler and Grove's (1992, 1993) model are plotted for comparison. Overall, there is a good agreement between our data and Kinzler and Grove's model, except that the liquids in equilibrium with ol + opx + cpx (+sp) in run FM1 at 1.25 GPa and FM2 at 1.0 GPa are slightly richer in diopside component and plot towards smaller melting degrees according to of Kinzler and Grove's (1992, 1993) parametrisation than the degrees measured in our experiments. This is probably due to the effect of source composition: our bulk composition FM has a higher CaO content and a smaller SiO_2 content than the MORB mantle source of Kinzler and Grove (1992, 1993). The main contribution of our experiments is to show that liquids in equilibrium with ol + opx (+sp) at low pressures (0.75 and 0.5 GPa; runs FM3 and FM4, respectively) plot even further away from the primitive MORB field, towards silica. The 0.5 GPa melt is indeed distinctly too rich in SiO_2

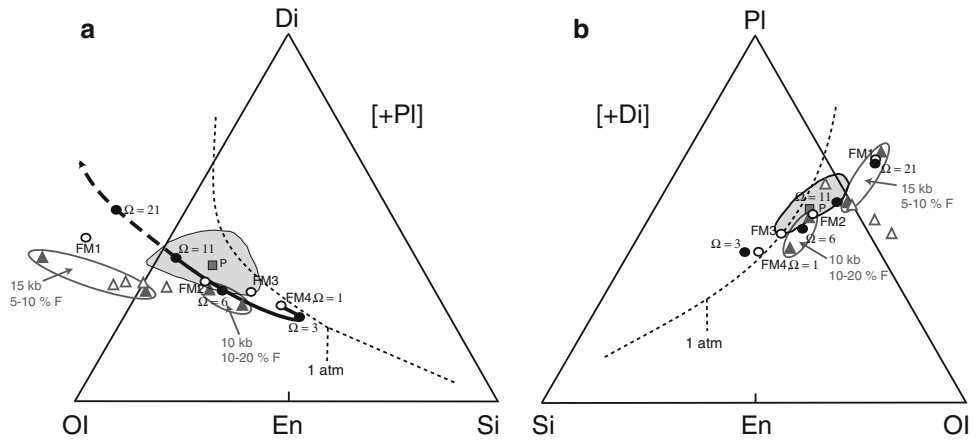

Fig. 10 Liquid compositions in partial melting experiments FM1 to FM4 (*empty circles*) and liquid compositions at $P = 0.5$ GPa and focusing factors equal to 3, 6, 11, and 21 (*solid circles*) projected in the olivine–diopside–silica–plagioclase tetrahedron. **a** Projection from plagioclase onto the plane olivine–diopside–silica; **b** projection from diopside onto the plane olivine–silica–plagioclase. The compositions at $\Omega = 11$ and 21 were computed with pMELTS. Liquid compositions produced by isobaric batch melting of spinel peridotite at 1.5 GPa and 1 are shown by *empty triangles*; they were computed using Kinzler and Grove's (1992, 1993) model for degrees of melting equal to 5 and 10% (at 1.5 GPa), and 10 and 20% (at 1 GPa). *Open triangles* correspond to aggregate magma compositions from a spinel lherzolite computed in the case of polybaric near-fractional melting using Kinzler's (1997) model; the calculations were made for 4 different mantle temperatures and yield oceanic crust thicknesses of 13, 9, 6 and 3 km (corresponding to initial pressures of melting of 3, 2.5, 2 and 1.5 GPa, respectively). The shaded area is the field of primitive MORBs (see Fig. 1), and point P is one of the most primitive MORB composition (ALV-519-4-1, Famous zone; Stolper 1980)

($\approx$52 wt%), and too poor in incompatible elements (TiO_2, Na_2O) in comparison to primitive MORBs (Fig. 7). Accordingly, equilibrium batch melting of mantle peridotite cannot produce primitive MORBs.

Current models of dynamic melting at mid-ocean ridges assume that MORBs are mixes of melts from all depths in the melting column, with an integrated total amount of melting around 10% (e.g., Klein and Langmuir 1987; McKenzie and Bickle 1988; Langmuir et al. 1992). Liquid compositions predicted in the case of polybaric, near-fractional melting of MORB mantle source (Kinzler 1997) are plotted in Fig. 10. The calculations correspond to various mantle temperatures (i.e., various initial pressures of melting) and yield with oceanic crust thicknesses ranging from 3 to 13 km. Kinzler's model shows that the major element variability of MORBs in terms of FeO, Na_2O and SiO_2 can be explained by a variable mantle temperature model. Nevertheless, it predicts aggregate melt compositions that are always too poor in diopside component in comparison with primitive MORBs (Fig. 10a) and it does not explain the opx undersaturation of MORBs. Indeed, as the instantaneous degrees of melting involved in dynamic melting models are relatively low, partial melts are saturated with opx over the whole depth of the melting column. Under certain circumstances, it is possible to mix opx-saturated liquids and obtain a liquid that is not saturated with opx (Asimow and Stolper 1999). However, this scenario is presumably not a general explanation to MORB generation as primitive MORBs are systematically and strongly opx-undersaturated. Also, the opx-undersaturated mixture should be somehow physically separated from host peridotites, otherwise it would evolve back to opx-saturation. Models of magma ascent by porous flow cannot satisfy for this requirement. In the case of porous flow, the liquid would indeed ascend slowly relative to the solid matrix, and closely approach chemical equilibrium with the mineral phases (e.g., Navon and Stolper 1987). Accordingly, taken alone, dynamic melting models cannot account for the fact that primitive MORBs are systematically undersaturated in opx.

The role of basalt-peridotite interactions in the generation of primitive MORBs

A number of studies were aimed at understanding the origin of the chemical difference between primitive MORBs and partial melts of mantle peridotites. Stolper (1980) explained this difference by olivine fractionation during magma ascent, which would drive partial melts formed at high pressures along ol + opx + cpx or ol + opx cotectic boundaries into the field of primitive MORBs (Fig. 1). More recently, Asimow and Stolper (1999) suggested that opx-undersaturation in primitive MORB compositions is acquired during focused magma transport in connection with the formation of highly permeable dunite channels at pressures $\geq$0.8 GPa. Our

experiments give further support to their conclusion as we show below.

Comparative evolution of liquid compositions at $\Omega = 1$ and $\Omega = 6$

To evaluate the effect of basalt–peridotite interactions on liquid compositions, we first compared the liquids produced at $\Omega = 1$ and $\Omega = 6$ as a function of the degree of melting. Between 1.25 and 0.75 GPa, decompression melting in composition FF6 consumes more opx and less cpx, and produces more ol than in mantle peridotite FM (Fig. 5). As a result, the liquids produced at a given P are enriched in silica and depleted in MgO and CaO (Fig. 6), and would plot even further away from the primitive MORB field than primary melts FM2 and FM3 in Fig. 10. This evolution towards the silica apex stops slightly below 0.75 GPa, when both opx and cpx disappear and the melting reaction switches from opx + cpx + sp = liquid + ol to ol (±sp) = liquid. Olivine dissolution results in a strong increase in MgO and decrease in SiO_2, CaO and Al_2O_3 concentrations in the liquid between 0.75 and 0.5 GPa (Fig. 6). Thus it drives the melt composition back towards the field of primitive MORBs (Fig. 10), suggesting a genetic relationship between the compositions of primitive MORBs and focused magma transport in dunite channels.

The behaviour of incompatible elements as a function of the focusing factor also indicates that basalt–peridotite interactions play a role in the formation of primitive MORBs. At all pressures between 1 and 0.5 GPa, Na_2O, TiO_2, and K_2O concentrations in liquids are much higher in series FF6 than in series FM, and approach the concentrations expected in primitive MORBs (Figs. 6, 7). To explain such enrichments, let us consider the case of K_2O, a focusing factor equal to 6, and let x be the mass fraction of K_2O in composition FM. Assuming that K_2O is perfectly incompatible, its mass fraction in the liquid in run FM1 is equal to x/f, where f is the melt fraction ($f = 0.088$; Table 2). Just after focusing, the mass of solid is equal to $1 - f$, and the mass of liquid to Ωf; the mass fraction of K_2O is equal to 0 in the solid, and to x/f in the liquid. Thus the mass fraction of K_2O in bulk composition FF6 is $\Omega x/(1 - f + \Omega f)$, that is $\approx 4.2x$ for $f = 0.088$ and $\Omega = 6$. Melt fractions in series FF6 are larger than in series FM (Fig. 5a), but always by a factor much lower than 4.2 so the liquids in series FF6 are strongly enriched in K_2O. At 0.5 GPa, for instance, the melt fraction is equal to 0.224 in sample FM4, and 0.510 in sample FF6-1. Accordingly, the mass fraction of K_2O in liquid in FF6-1 should be 1.84 times larger than in FM4: $4.2x/0.510$ in FF6-1 versus $x/0.224$ in FM4. In fact, K_2O is 1.90 times larger in run FF6-1 (0.40 wt%; Table 3) than in run FM4 (0.21 wt%) (Table 3), in perfect agreement with our theoretical estimate.

Evolution of 0.5 GPa liquid compositions with increasing Ω

In our model (Fig. 2), we assumed that the main transport mechanism switches from porous flow into highly permeable channels to magma transport in dikes at some low pressure (fixed to 0.5 GPa in the experiments). We also supposed that primitive MORBs correspond to liquids last equilibrated with ol (±sp) in the upper part of the highly permeable channels, and then rapidly transported to the surface without significant modifications. In this section, we try to constrain the range of focusing factors necessary to produce at 0.5 GPa liquids that match the compositions of primitive MORBs.

In the olivine–silica–diopside–plagioclase tetrahedron (Fig. 10), the liquid compositions at 0.5 GPa and Ω ranging from 1 to 21 show a complex evolutionary trend, with two fields:

1. For Ω increasing from 1 to 3, we notice a strong increase of SiO_2 from 51.9 to 53.4 wt% and decreases of MgO and CaO (Fig. 6), due to the growing contribution of opx to melting. As a result, the liquid moves away from the primitive MORB field towards the silica apex in Fig. 10. Also, opx is still stable at $\Omega = 3$ and $P = 0.5$ GPa. Accordingly, a focusing factor >3 is required to consume all opx at 0.5 GPa, and to produce liquids approaching primitive MORBs.
2. Orthopyroxene disappears at a value of Ω somewhere between 3 and 6 ($\Omega = 4$ according to pMELTS), and thereafter liquid is in equilibrium with ol only. A complete reversal of the liquid trend towards primitive MORBs is observed in connection with the disappearance of opx (Fig. 10), with major increases of MgO and FeO, and a decrease of SiO_2 due to the effect of ol dissolution at $\Omega = 6$. Nevertheless, the liquid at $\Omega = 6$ is again too rich in SiO_2 and too poor in FeO in comparison with primitive MORBs. This is mainly due to the low pressure of equilibration (0.5 GPa) considered in this study. Indeed, the compositions computed for liquid in equilibrium with ol (±sp) only at 0.75 GPa and 1 GPa (FF′7 and FF′23, respectively; Table 4) have lower SiO_2 and higher FeO contents. This is consistent with the strong control exerted by pressure on melt composition, especially the SiO_2 and FeO contents, as established by Langmuir et al. (1992). The liquid composition computed for $\Omega = 11$ plots right in the primitive MORB field (Fig. 10). Note also that Na_2O, K_2O, and TiO_2 increase continuously with increasing Ω, and that concentrations of Na_2O and

TiO_2 at $\Omega = 6$ and 11 are consistent with those expected for primitive MORBs (Fig. 7). For $\Omega \geq 11$, the liquid is always in equilibrium with ol only, but the melt composition seems to be mostly controlled by the dilution effect due to the added liquid in the system. Hence, oxide concentrations would evolve to the composition of synthetic basalt (Table 1): MgO, SiO_2 and Cr_2O_3 decrease and TiO_2, Al_2O_3 and alkalis increase (Fig. 7) with increasing Ω. For $\Omega = 21$, liquid composition is nepheline-normative and plots well beyond the olivine–diopside join in the field of alkali basalts (Fig. 10).

In the ol + liquid field ($\Omega \geq 4$ at $P = 0.5$ GPa), the evolution of liquid composition is controlled by two vectors (Fig. 11): the focusing vector, which embodies the change of the bulk composition of the system from FM at $\Omega = 1$ to the composition of the "contaminant" (that is, the liquid added to the system at focusing level) at $\Omega \rightarrow \infty$; and the olivine fractionation vector. For $\Omega = 11$, for instance, the magma/rock ratio is equal to $(\Omega - 1)f = 0.88$. At any temperature between the olivine liquidus and the crystallization temperature of the next solid phase (cpx, sp or plagioclase, depending on pressure and bulk composition), the system is composed of ol + liquid only, and the liquid composition lies somewhere along the ol fractionation vector: the lower the temperature, the further away from the ol apex. The main point is that the ol fractionation vector for bulk composition FF11 goes through the field of primitive MORBs. Using this construction, it is possible to bracket the magma/rock ratios required to produce primitive MORBs (Fig. 11): primitive MORBs with the highest normative hyperstene content should correspond to a magma/rock ratio of ≈ 0.32 ($\Omega = 4.6$), and those slightly nepheline-normative to a magma/rock ratio of ≈ 1.06 ($\Omega = 13.1$).

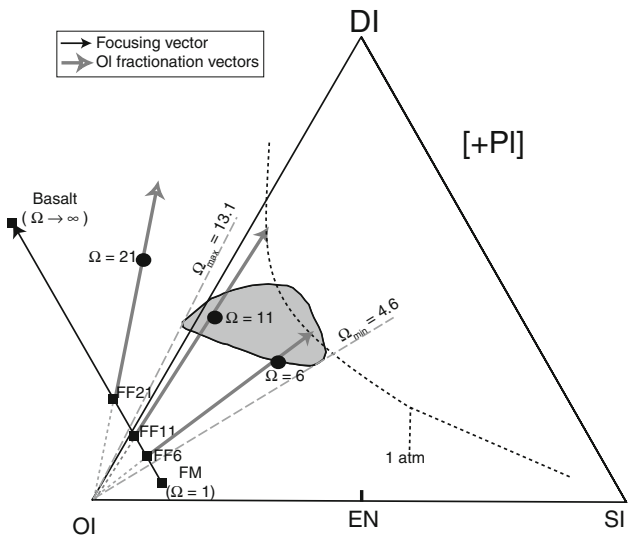

Fig. 11 Basalt–peridotite interactions and the genesis of primitive MORBs and dunite channels (compositions are projected from plagioclase onto the plane olivine–diopside–silica). At $P = 0.5$ GPa and $\Omega \geq 4$, liquid is in equilibrium with ol only and its evolution is controlled by two vectors: (1) the focusing vector, which encompasses the range of bulk compositions from FM at $\Omega = 1$ to the composition of the "contaminant" (the liquid in run FM1) at $\Omega \rightarrow \infty$; and (2) the olivine fractionation vector. The ol fractionation vector for bulk composition FF11 goes through the field of primitive MORBs (the position of the liquid along this vector depends on temperature, which controls the amount of olivine). Focusing factors ≤ 4.6 will yield compositions too rich in normative hyperstene to be primitive MORBs, and factors ≥ 13.1 compositions too rich in normative nepheline, such as the liquid computed for $\Omega = 21$

Summary and implications

Our experiments show that the interactions between ascending magmas and host peridotites can lead to conditions where liquids are in equilibrium with ol only and acquire compositions matching those of primitive MORBs. The effects of these interactions on phase relations and compositions, and on the generation of dunite rock-types may be summarised as follows:

1. Our experiments confirm that decompression melting of lherzolites cannot fully consume opx and produce dunite residues, even at 0.5 GPa. On the contrary, complete exhaustion of opx (and cpx) can readily be achieved in the case of focused magma ascent. Magma focusing induces indeed major changes of the coefficients of the melting reaction, in particular, a major increase of the rate of opx consumption.
2. The pressure P_{Dunite}, at which a dunite residue is formed, is strongly dependent on the focusing factor. In the investigated systems, factors equal to ≈ 4 and 8—that is, magma/rock ratios equal to ≈ 0.26 and 0.62—are required to form dunites at 0.5 and 0.8 GPa, respectively. Very large focusing factors would be necessary to produce a dunite at higher pressures ($\Omega = 23$ for $P_{\text{Dunite}} = 1$ GPa).
3. Basalt–peridotite interactions have strong effects on the modal and major element compositions of residues. They can yield residual rocks with low pyroxene abundances (and in some cases, cpx > opx) that are very depleted in SiO_2, CaO, Al_2O_3, and enriched in MgO and FeO, in comparison to the residues of closed-system partial melting of peridotites. The geochemical variability of some peridotite suites could result from a combination of partial melting, melt extraction, and magma-rock interactions.
4. Liquids produced in equilibrium with ol (±sp) at low pressure (0.5 GPa) in highly permeable channels have lower SiO_2 concentrations, and higher concentrations in MgO, FeO, and incompatible elements (Na_2O, K_2O,

TiO_2) than liquids produced by decompression melting of the fertile mantle (at the same *P*–*T* conditions), and plot in the primitive MORB field in the olivine–silica–diopside–plagioclase tetrahedron. In this study, magma/rock ratios in the range 0.3–1.1 are required to produce primitive MORB compositions at 0.5 GPa. In nature, these ratios will depend on the pressure and melt composition at the focusing level(s), and on the final pressure at which the partial melt is extracted from the dunite residue to form dikes.

Hence, our experiments and calculations confirm that there is a genetic relationship between focused magma ascent, dunite bodies in the upper mantle, and the generation of primitive MORBs (Asimow and Stolper 1999). Dynamic melting and pervasive porous flow would dominate in the lower part of the melting zone beneath mid-ocean ridges, but focused magma transport into highly permeable channels would take place at some intermediate depth, as sketched in Fig. 2, and modify to a variable extent the composition of melts produced by dynamic melting. In this frame, the composition of primitive MORBs is controlled by two main mechanisms: (a) the change of the bulk composition of the system due to the addition of liquid at the focusing level (as represented by the focusing vector in Fig. 11); and (b) ol–liquid equilibrium into dunite channels (as represented by the ol fractionation vectors in Fig. 11). The implications for global variations of MORB compositions (Langmuir et al. 1992) are beyond the scope of this paper. Nevertheless, it is interesting to note that mechanism (a) can lead to significant geochemical changes, unrelated to variations of potential temperature, average degree of melting, or mantle composition. In particular, large variations of the concentrations in incompatible elements, such as Na_2O, can be produced by changes in the focusing factor, at constant potential temperature of the mantle (Fig. 6).

Finally, we want to point out a possible relationship between focused magma transport in dunite channels and the large ol phenocrysts containing geochemically contrasted melt inclusions that have been described in MORBs (e.g., Sobolev and Shimizu 1993; Shimizu 1998; Laubier et al. 2007). These melt inclusions have been interpreted as sampling a range of liquids coming from different sources and/or produced by different degrees of melting of a single source: almost all the liquids would be mixed and homogenised in a shallow magma chamber to yield the erupted lavas, but small liquid volumes would somehow get trapped into growing ol phenocrysts, and thus escape homogenisation. Interestingly, a single high-permeability channel—particularly in the case of a branching network of channels, as proposed by Hart (1993)—may focus liquids coming from different sources (or different degrees of melting of the same source) and having contrasted major and trace element compositions or isotopic signatures: the only requirement is that all these liquids must be in equilibrium with a high Ol-Mg# (typically, 90–92). Accordingly, we suggest that the upper part of dunite channels, where the main magma transport mechanism switches from porous flow to dike ascent, is one place where large ol crystals containing geochemically contrasted melt inclusions may be produced and later incorporated into ascending magmas.

Conclusion

We performed piston-cylinder experiments to study the reaction between ascending magmas and host peridotites beneath mid-ocean ridges, and to evaluate the effect of *P*, *T*, and magma/rock ratio on the composition and proportions of reaction products. Our experiments show that basalt–peridotite interactions in highly permeable channels can lead to the formation of primitive MORB-like liquids in equilibrium with a dunitic residue. Hence our study gives further support to the assumption (e.g., Kelemen et al. 1995; Asimow and Stolper 1999) that magma transport by focused flow can explain both the formation of dunite channels beneath mid-ocean ridges and the generation of primitive MORBs. Accordingly, the degree of peridotite-melt interactions is an additional parameter that must be taken in account, in the interpretation of the chemical variability of MORBs.

Finally, we want to emphasise that more systematic experimental studies are required to better constrain the effects of basalt–peridotite interactions. In particular, one question that deserves more attention is how the focusing pressure, which controls the composition of liquid added to the fertile mantle, affects the evolution of liquid compositions with decreasing pressure and the formation of dunites.

Acknowledgments This study has benefited from discussions with Andréa Tommasi, Marguerite Godard and Muriel Laubier. Special thanks are due to the following persons: Jean-Luc Devidal for technical assistance with the electron microprobe; Jean-Marc Hénot for technical assistance with the scanning electron microscope; Ariel Provost for his mass-balance program; Kenneth Koga for assistance with algorithm pMELTS; Mhammed Benbakkar for the ICP-AES analysis of the synthetic basalt in Table 1. This study was supported by the program DyETI of the Institut National des Sciences de l'Univers (INSU-CNRS), through grants to D. Laporte and A. Tommasi. Many thanks to T. L. Grove and two anonymous reviewers for their constructive comments.

References

Albarède F, Provost A (1977) Petrological and geochemical mass-balance equations: an algorithm for least-square fitting and general error analysis. Comput Geosci 3:309–326. doi:10.1016/0098-3004(77)90007-3

Ancey M, Bastenaire F, Tixier R (1978) Application des méthodes statistiques en microanalyse. In: Maurice F, Meny L, Tixier R (eds) Microanalyse, microscopie électronique à balayage. Les éditions du Physicien, Orsay, pp 323–347

Asimow PD, Stolper EM (1999) Steady-state mantle-melt interactions in one dimension: equilibrium, transport and melt focusing. J Petrol 40(3):475–494. doi:10.1093/petrology/40.3.475

Asimow PD, Hirschmann MM, Stolper EM (2001) Calculations of peridotite partial melting from thermodynamic models of minerals and melts, IV. Adiabatic decompression and the composition and mean properties of Mid-ocean Ridge Basalts. J Petrol 42(5):963–998. doi:10.1093/petrology/42.5.963

Baker MB, Stolper EM (1994) Determining the composition of high-pressure mantle melts using diamond aggregates. Geochim Cosmochim Acta 58:2811–2827. doi:10.1016/0016-7037(94)90116-3

Baker MB, Beckett JR (1999) The origin of abyssal peridotite: a reinterpretation of constraints based on primary bulk composition. Earth Planet Sci Lett 171:49–61. doi:10.1016/S0012-821X(99)00130-2

Bedini RM, Bodinier JL, Vernieres J (2002) Numerical simulation of Mg–Fe partitioning during melting and melt-rock interactions in the shallow upper mantle. Orogenic Lherzolite Conference, Abstract Volume, Japan 2002

Braun MG (2004) Petrologic and microstructural constraints on focused melt transport in dunites and the rheology of the shallow mantle. PhD Thesis, Massachusetts Institute of Technology

Braun MG, Kelemen PB (2002) Dunite distribution in the Oman Ophiolite: implications for melt flux through porous dunite conduits. Geochem Geophys Geosyst. doi:10.1029/2001GC000289

Christie DM, Carmichael ISE, Langmuir CH (1986) Oxidation states of mid-ocean ridge basalt glasses. Earth Planet Sci Lett 79:397–411. doi:10.1016/0012-821X(86)90195-0

Daines MJ, Kohlstedt DL (1994) The transition from porous to channelized flow due to melt/rock reaction during melt migration. Geophys Res Lett 21:145–148. doi:10.1029/93GL03052

Dick HJB (1989) Abyssal peridotites, very slow spreading ridges and ocean ridge magmatism. In: Saunders AD, Norry MJ (eds) Magmatism in the ocean basins. Geol Soc Spec Publ, London 42:71–105

Elthon D (1979) High magnesia liquids as the parental magma for ocean floor basalts. Nature 278:514–518. doi:10.1038/278514a0

Elthon D (1987) Petrology of gabbroic rocks from the mid-Cayman Rise spreading center. J Geophys Res 92:658–682. doi:10.1029/JB092iB01p00658

Elthon D (1989) Pressure of origin of primary mid-ocean ridge basalts. In: Saunders AD, Norry MJ (eds) Magmatism in the ocean basins. Geol Soc of Am, Boulder, pp 125–136

Elthon D, Scarfe CM (1980) High-pressure phase equilibria of a high-magnesia basalt: implications for the origin of mid-ocean ridge basalts. Can Inst Wa Yrbk, pp 277–281

Elthon D, Scarfe CM (1984) High-pressure phase equilibria of a high-magnesia basalt and the genesis of primary oceanic basalts. Am Mineral 69:1–15

Ghiorso MS, Sack RO (1995) Chemical mass transfer in magmatic processes IV. A revised and internally consistent thermodynamic model for the interpolation and extrapolation of liquid-solid equilibria in magmatic systems at elevated temperatures and pressures. Contrib Mineral Petrol 119(2/3):197–212. doi:10.1007/BF00307281

Ghiorso MS, Hirschmann MM, Reiners PW, Kress VC (2002) The pMELTS: a revision of MELTS for improved calculation of phase relations and major element partitioning related to partial melting of the mantle to 3 GPA. Geochem Geophys Geosyst. doi:10.1029/2001GC000217

Godard M, Bodinier JL, Vasseur G (1995) Effects of mineralogical reactions on trace element redistributions in mantle rocks during percolation processes: a chromatographic approach. Earth Planet Sci Lett 133:449–461. doi:10.1016/0012-821X(95)00104-K

Green DH, Hibberson WO, Jaques AL (1979) Petrogenesis of mid-ocean ridge basalts. In: McElhinney MW (ed) The earth: its origin, structure and evolution. Academic Press, London

Hart SR (1993) Equilibration during mantle melting: a fractal tree model. Proc Natl Acad Sci USA 90:11914–11918. doi:10.1073/pnas.90.24.11914

Jackson MD, Ohnenstetter M (1981) Peridotite and gabbroic structures in the Monte Maggiore Massif, Alpine Corsica. J Geol 89:703–719

Hess PC (1992) Phase equilibria constraints on the Origin of Ocan Floor Basalts. Am Geophys Union Monogr 71:67–102

Kelemen PB, Joyce DB, Webster JD, Holloway JR (1990) Reaction between ultramafic wall rock and fractionating basaltic magma: Part II, Experimental investigation of reaction between olivine tholeiite and harzburgite at 1150 and 1050°C and 5 kbar. J Petrol 31:99–134

Kelemen PB, Shimizu N, Salters VJM (1995) Extraction of mid-ocean-ridge basalt from the upwelling mantle by focused flow of melt in dunite channels. Nature 375:747–753. doi:10.1038/375747a0

Kelemen PB, Hirth G, Shimizu N, Spiegelman M, Dick HJB (1997) A review of melts migration processes in the adiabatically upwelling mantle beneath oceanic spreading ridges. Philos Trans R Soc Lond A 355:283–318. doi:10.1098/rsta.1997.0010

Kinzler RJ (1997) Melting of mantle peridotite at pressures approaching the spinel to garnet transition: application to mid-ocean ridge basalt petrogenesis. J Geophys Res 102:853–874. doi:10.1029/96JB00988

Kinzler RJ, Grove TL (1992) Primary magmas of mid-ocean ridge basalts 2. Applications. J Geophys Res 97:6907–6926. doi:10.1029/91JB02841

Kinzler RJ, Grove TL (1993) Corrections and further discussion of the primary magmas of mid-ocean ridge basalts, 1 and 2. J Geophys Res 98:22339–22347. doi:10.1029/93JB02164

Klein EM, Langmuir CH (1987) Global correlations of ocean ridge basalt chemistry with axial depth and crustal thickness. J Geophys Res 92:8089–8115. doi:10.1029/JB092iB08p08089

Kogiso T, Hirose K, Takahashi E (1998) Melting experiments on homogeneous mixtures of peridotite and basalt: application to the genesis of ocean island basalts. Earth Planet Sci Lett 162:45–61. doi:10.1016/S0012-821X(98)00156-3

Kubo K (2002) Dunite formation processes in highly depleted peridotite: Case study of the Iwanaidake, Hokkaido, Japan. J Petrol 43:423–448. doi:10.1093/petrology/43.3.423

Langmuir CH, Klein EM, Plank T (1992) Petrological systematics of mid-ocean ridge basalts: constraints on melt generation beneath ocean ridges. Am Geophys Union Monogr 71:183–280

Laporte D, Toplis MJ, Seyler M, Devidal JL (2004) A new experimental technique for extracting liquids from peridotite at very low degrees of melting: application to partial melting of depleted peridotite. Contrib Mineral Petrol 146:463–484. doi:10.1007/s00410-003-0509-3

Laporte D, Schiano P, Boivin P (2006) The composition of low degree melts of fertile peridotites at 1 and 1.3 GPa. EMPG XI (XIth International Symposium on Experimental Mineralogy, Petrology and Geochemistry), Bristol

Laubier M, Schiano P, Doucelance R, Ottolini L, Laporte D (2007) Olivine-hosted melt inclusions and melting processes beneath the famous zone (mid-atlantic ridge). Chem Geol 240:129–150. doi:10.1016/j.chemgeo.2007.02.002

McKenzie D, Bickle MJ (1988) The volume and composition of melt generated by extension of the lithosphere. J Petrol 29:625–697

McKenzie D, O'Nions RK (1991) Partial melt distributions from inversion of rare Earth element concentrations. J Petrol 32:1021–1091

Morgan Z, Liang Y (2003) An experimental study of the kinetics of harzburgite reactive dissolution with applications to dunite dike formation. Earth Planet Sci Lett 214:59–74. doi:10.1016/S0012-821X(03)00375-3

Morgan Z, Liang Y (2005) An experimental study of the kinetics of lhezolite reactive dissolution with applications to dunite dike formation. Contrib Mineral Petrol 150:369–385. doi:10.1007/s00410-005-0033-8

Navon O, Stolper EM (1987) Geochemical consequences of melt percolation–the upper mantle as a chromatographic column. J Geol 95:285–307

Niu Y (1997) Mantle melting and melt extraction processes beneath Ocean Ridges: evidence from abyssal peridotites. J Petrol 38:1047–1074. doi:10.1093/petrology/38.8.1047

Niu Y, Hékinian R (1997) Spreading-rate dependence of the extent of mantle melting beneath ocean ridges. Nature 385:326–329. doi:10.1038/385326a0

Niu Y, Langmuir CH, Kinzler RJ (1997) The origin of abyssal peridotites: a new perspective. Earth Planet Sci Lett 152:251–265. doi:10.1016/S0012-821X(97)00119-2

O'Hara MJ (1965) Primary magmas and the origin of basalts. Scot J Geol 1:19–40

O'Hara MJ (1968) Are ocean floor basalts primary magma? Nature 220:683–686. doi:10.1038/220683a0

O'Hara MJ (1977) Geochemical evolution during fractional crystallization of a periodically refilled magma chamber. Nature 266:503–507. doi:10.1038/266503a0

O'Hara MJ, Mathews RE (1981) Geochemical evolution in a advancing periodically replenished, periodically tapped, continuously fractionated magma chamber. J Geol Soc Lond 138:237–277. doi:10.1144/gsjgs.138.3.0237

Quick JE (1981) The origin and significance of large, tabular dunite bodies in the Trinity peridotite, northern California. Contrib Mineral Petrol 78:413–422. doi:10.1007/BF00375203

Rampone E, Romairone A, Hofmann AW (2004) Contrasting bulk and mineral chemistry in depleted mantle peridotites: evidence for reactive porous flow. Earth Planet Sci Lett 218:491–506. doi:10.1016/S0012-821X(03)00679-4

Shimizu N (1998) The geochemistry of olivine-hosted melt inclusions in a Famous basalt ALV519–4-1. Phys Earth Planet Int 107:183–201. doi:10.1016/S0031-9201(97)00133-7

Sobolev AV, Shimizu N (1993) Ultra-depleted primary melt included in an olivine from the Mid-Atlantic Ridge. Nature 363:151–154. doi:10.1038/363151a0

Spiegelman M, Kelemen PB, Aharonov E (2001) Causes and consequences of flow organization during melt transport: The reaction infiltration instability in compactible media. J Geophys Res 106(B2):2061–2077. doi:10.1029/2000JB900240

Stolper E (1980) A phase diagram for mid-ocean ridge basalts: preliminary results and implications for petrogenesis. Contrib Mineral Petrol 74(1):13–27. doi:10.1007/BF00375485

Suhr G (1999) Melt migration under oceanic ridges: inferences from reactive modelling of upper mantle hosted dunites. J Petrol 40:575–599. doi:10.1093/petrology/40.4.575

Suhr G, Hellebrand E, Snow JE, Seck HA, Hofmann AW (2003) Significance of large, refractory dunite bodies in the upper mantle of the Bay of Islands Ophiolite. Geochem Geophys Geosyst. doi:10.1029/2001GC000277

Takahashi N (1992) Evidence for melt segregation towards fractures in Horoman mantle peridotite complex. Nature 359:52–58. doi:10.1038/359052a0

Tommasi A, Godard M, Coromina G, Dautria JM, Barsczus H (2004) Seismic anisotropy and compositionally induced velocity anomalies in the lithosphere above mantle plumes: a petrological and microstructural study of mantle xenoliths from French Polynesia. Earth Planet Sci Lett 227:539–556. doi:10.1016/j.epsl.2004.09.019

Walker D, Shibata T, Delong SE (1979) Abyssal tholeiites from the Oceanographer Fracture Zone II. Phase equilibria and mixing. Contrib Mineral Petrol 71:111–125. doi:10.1007/BF00374440

Yaxley (2000) Experimental study of the phase and melting relations of homogeneous basalt + peridotite mixtures and implications for the petrogenesis of flood basalts. Contrib Mineral Petrol 139:326–338

Yoder HS (1976) Generation of basaltic magma. Natl Acad Sci, Washington DC, pp 143–144